Title
Orientation of Calcium Silicate Hydrate Nanoparticles under Shear Deformations

Author
Su, Ying-Tsun

Publication Date
2021

Peer reviewed|Thesis/dissertation

Orientation of Calcium Silicate Hydrate Nanoparticles under Shear Deformations

By

Ying-Tsun Su

A dissertation submitted in partial satisfaction of the

requirements for the degree of

Doctor of Philosophy

in

Applied Science & Technology

in the

Graduate Division

of the

University of California, Berkeley

Committee in charge:

Professor Paulo J. M. Monteiro, Chair
Professor Hans-Rudolf Wenk
Professor Lisa A. Pruitt

Fall 2021

Orientation of Calcium Silicate Hydrate Nanoparticles under Shear Deformations

Abstract

Orientation of Calcium Silicate Hydrate Nanoparticles under Shear Deformations

by

Ying-Tsun Su

Doctor of Philosophy in Applied Science & Technology

University of California, Berkeley

Professor Paulo J. M. Monteiro, Chair

Concrete is one of the most widely used engineering materials worldwide, significantly exceeding any other infrastructure material, such as steel and wood. At present, most of the feasible options for microstructural improvement of cement and concrete have been implemented. Thus, there is an urgent need to find scientific and technically-viable improvements by engineering the cementitious phases at the nanometer scale to increase concrete strength and durability. Calcium silicate hydrate (C-S-H) is the main hydration product of Portland cement and the principal binding agent in the cement paste; as such, C-S-H is the main contributor to the mechanical properties of concrete.

Monteiro lab has previously performed high-pressure x-ray diffraction (HP-XRD) experiments on calcium (alumino)silicate hydrate (C-(A-)S-H), a structurally similar material as C-S-H, using diamond anvil cell (DAC). The results from these studies confirm the hypothesis that fiber-like C-(A-)S-H nanoparticles will preferentially orient to the compression direction under uniaxial deformation, and no texture will form under hydrostatic stresses. However, owing to the lack of control of applied loads in the DAC, where each incremental loading (or unloading) is typically in the order of GPa, it is necessary to perform the experiments under more relevant and realistic conditions, i.e., with applied loads in the order of MPa, for studying mechanical properties of cement paste and concrete. To better control the loading pressures, this research uses deformation-DIA (D-DIA) multi-anvil apparatus and large-volume press (LVP) system at beamline 13-BM-D of Advanced Photon Source to conduct in situ shear deformation experiments and measure the orientation behaviors of C-S-H with x-ray diffractions.

The first goal of this dissertation aims to investigate the rearrangement of C-S-H nanoparticles under shear stresses, which has been postulated to be a potential root cause of concrete creep. Furthermore, the structure of C-S-H nanoparticles is modified with (3-aminopropyl)triethoxysilane (APTES) and polycarboxylate ethers (PCEs), and the goal is to examine the effects on the texture of these modified nanocomposites.

The x-ray diffraction results reveal the structural modifications of C-S-H via intercalations of different organic contents. The bulk modulus of these modified-CSH nanocomposites was computed using the Birch-Murnaghan equation of state. The results show that the intercalations of small organic molecules APTES produce more chemically stable and higher bulk modulus C-S-H nanocomposites than the intercalations of C-S-H with PCEs.

The results from the high-pressure x-ray diffraction experiments at beamline 13-BM-D show for the first time that C-S-H nanoparticles could start forming texture at deviatoric stress of around 120 MPa and could represent the energy barrier for the initiation process of the C-S-H nanoparticles' orientations under shear loading. In a separate cyclic loading experiment, x-ray radiography images capture the delay in strain response of C-S-H under shear loading; the results may be the first direct measurements from the experiment that show the viscous nature of C-S-H, which is linked to concrete creep.

Finally, the results from the shear deformation experiments on the modified C-S-H structure demonstrate that CSH-APTES nanocomposites show more resistance to developing preferred orientations under deviatoric stresses than unmodified C-S-H samples. Higher deviatoric stresses are also required to drive the "initiation" process of forming textures for CSH-APTES nanocomposites compared to unmodified C-S-H nanoparticles.

The studies from these experiments open up a new chapter in understanding the cementitious phase at the nanometer scale. In particular, if rearrangement of C-S-H nanoparticles is the root cause of concrete creep, then the development of creep may be monitored by HP-XRD techniques. The results also show that the intercalations of small organic molecules into the layered structure of C-S-H could effectively design a more creep-resistant concrete. These structural modifications help us better understand C-S-H's structure-property relationships and provide a promising strategy for designing C-S-H to resist creep from the bottom-up approach.

Table of Contents

Figures

Tables

Acknowledgment

I want to thank my family for their support and unconditional love throughout this journey. They have encouraged me to pursue my passion and dream whenever I hesitate. And they always provide me the wisdom to accomplish the challenges that I face along the way.

I am honored to be a student in the Monteiro Lab and have Professor Monteiro be my research advisor. Professor Monteiro is one of the most respectful people I have ever met, not only because of his extraordinary achievements in academia but also his deep caring about my well-being outside of the research. It is truly an honor and great pleasure to be his student.

In addition, I want to thank Professor Wenk and Professor Pruitt especially; they always provide insightful advice and mentoring whenever I need guidance. And they always welcome me to their offices and classes/group meetings to discuss my research or any personal matters I might have.

Last but not least, I want to thank all the friends, staff, and professors that I had the chance to meet and work with at Berkeley, Advanced Light Source, and Advanced Photon Source. They have provided the supports and inspiration that help me to succeed during my Ph.D. research.

Thank you!

Chapter One: Introduction

1.1 Motivation and Research Goals

Concrete is one of the most widely used engineering materials worldwide, significantly exceeding any other infrastructure material, such as steel and wood, on a per capita basis [1]. The production of Portland cement, which is the main component of concrete that provides cohesive forces to "glue" aggregates, is estimated to account for 8-9% of the emission of CO_2 and 2-3% of total energy use worldwide and raises substantial environmental concerns [1]. With the ever-increasing demand, there is an urgent need to find scientific and technically viable improvements to manufacture more sustainable concrete.

In the past few decades, researchers have constantly attempted to increase the sustainability of cement and concrete by investigating structure-property relationships of the material. However, most of the feasible options for microstructural improvement of the concrete have been implemented. Furthermore, concrete creep remains a longstanding problem for the civil infrastructure despite numerous efforts of research; concrete creep is responsible for an estimated 78.8 billion dollars of maintenance costs for the highway and bridge in the United States alone [2], yet, the root cause and the mechanisms of concrete creep are still not fully understood.

One potential solution to enhance the mechanical properties of concrete, such as strength and durability, is by engineering the cementitious phases at atomic and nanometer scales. For example, Van Damme et al. [3] adopt a biomimetic approach to synthesize organic-inorganic nanocomposite materials to improve the inherently brittle natures of cement and concrete. The authors also use atomic-scale simulations by ab initio and molecular dynamics and engineer the bonding scheme in C-S-H to fine-tune the mechanical properties of cementitious materials.

The focus of this work is on calcium silicate hydrate, the main hydration product of Portland cement, and commonly abbreviated as C-S-H (or C-(A-)S-H if the structure contains Aluminum-substituted "dreierketten"-type silicate chains). In the cementitious matrix, calcium silicate hydrate forms up to approximately 60% by volume. It is the principal binding agent in the cement paste, contributing the most to a concrete's mechanical properties and long-term performance [4]. The goal of this research is twofold. First, many theories and models hypothesize that the rearrangement of C-S-H nanoparticles under deviatoric stresses is responsible for concrete creep. This research project aims to apply high-pressure x-ray diffraction techniques and experimentally measure synthetic C-S-H nanoparticles' orientation under deviatoric stresses. Second, the structure of C-S-H nanoparticles will be modified with organic molecules to form organic-inorganic nanocomposites. The goal is to better understand the effect of the structural modification on C-S-H when subject to the deviatoric stresses and thus provide more insights for designing a more creep-resistant concrete.

In the following sections, the structure of C-S-H and the proposed creep mechanisms of C-S-H will be reviewed.

1.2 Structure of C-S-H

Over the years, researchers made numerous efforts to examine the structure of C-S-H. In 1986, Taylor proposed that the disordered layer structure of C-S-H is an analog of structurally imperfect 1.4 nm tobermorite and jennite, and often referred to as C-S-H (I) and C-S-H (II), respectively in the literature [5]. Figure 1 shows the proposed C-S-H structure by Taylor. Different calcium to silicon ratios (Ca/Si ratio) could form different silicate chain lengths in this model. Furthermore, Al^{3+} ions can substitute into Si^{4+} tetrahedra due to similar ionic radii but may only do so in those bridging tetrahedra.

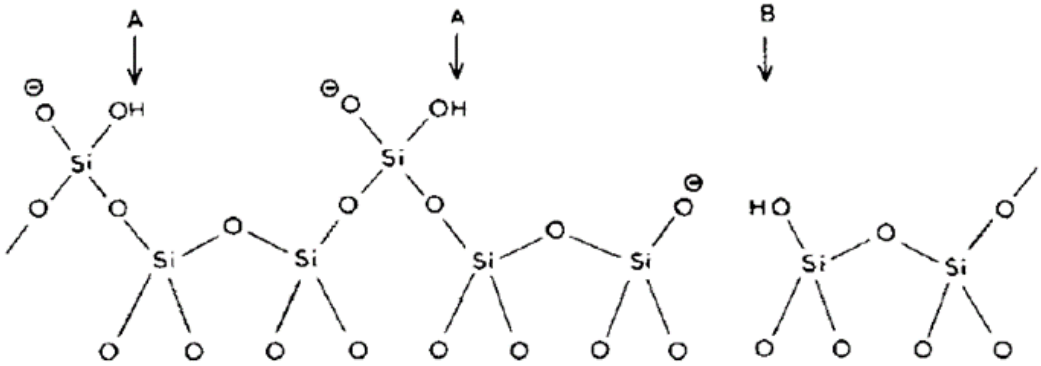

Figure 1 Proposed C-S-H structure based on silicate chain present in jennite and 1.4 nm tobermorite [5]

In the early 2000s, Merlino et al. solved the crystal structures of riversideite, tobermorite, and plombierite, each structure has characteristic basal spacings of 9 Å, 11 Å, and 14 Å, respectively, and these mineral crystal structures are often used as the starting model for C-S-H structure refinements in x-ray diffraction experiments [6, 7]. Figure 2 is a schematic diagram showing structures of C-S-H modified from tobermorite (infinite chain-length silicates) [8].

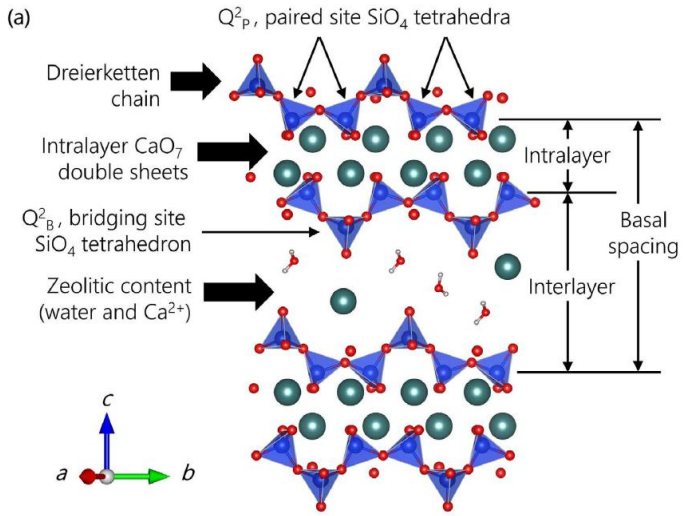

Figure 2 Schematic diagrams showing structures of C-S-H modified from tobermorite [8]

In 2007, Jennings proposed one of the most widely accepted models for C-S-H by combining small-angle neutron and x-ray scattering data. This model treats C-S-H as an aggregation of precipitated colloidal-size nanoparticles, as shown in Figure 3 [9]. However, despite its success in matching the data with scattering experiments, the authors did not provide a detailed explanation to address why these colloidal-size nanoparticles remain their characteristic length scale at ~5 nm and do not grow into larger-size nanoparticles [10].

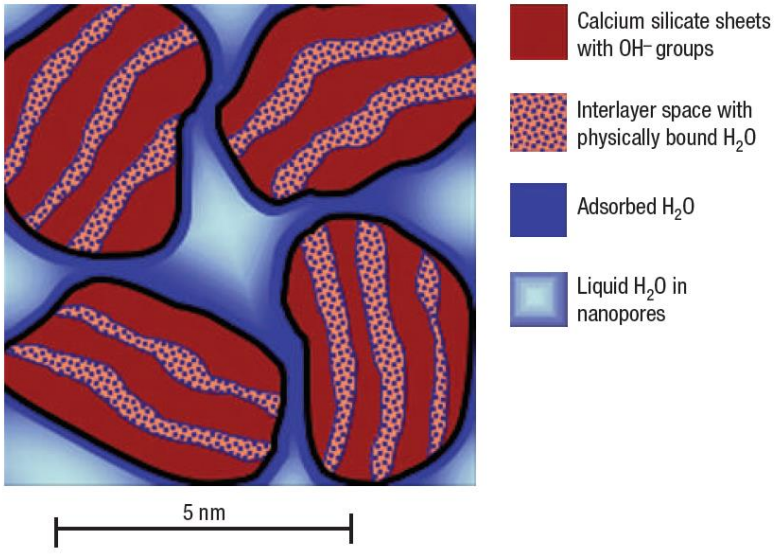

Figure 3 Illustrations of C-S-H nanoparticles with interlayered and adsorbed waters based on small-angle neutron and x-ray scatterings [9]

In 2008, Stemmermann et al. used synchrotron x-ray to systematically study structural changes of C-S-H with various Ca/Si ratios [11]. Morphologies of C-S-H synthesized by the reactions of silica with lime and hydration of tricalcium silicate have also been studied and compared by Richardson using transmission electron microscopy more recently [12]. Richardson shows that C-S-H sample synthesized from $CaO\text{-}SiO_2$ solutions contain only fiber-like morphology, regardless of Ca/Si ratios (top row in Figure 4); on the other hand, morphologies of C-S-H formed via hydration of tricalcium silicate depend on the molar concentration of CaO but did not depend on kinetics of the reactions. The structure can vary from foil-like to fibrillar-like or a mixture of the two (bottom row in Figure 4).

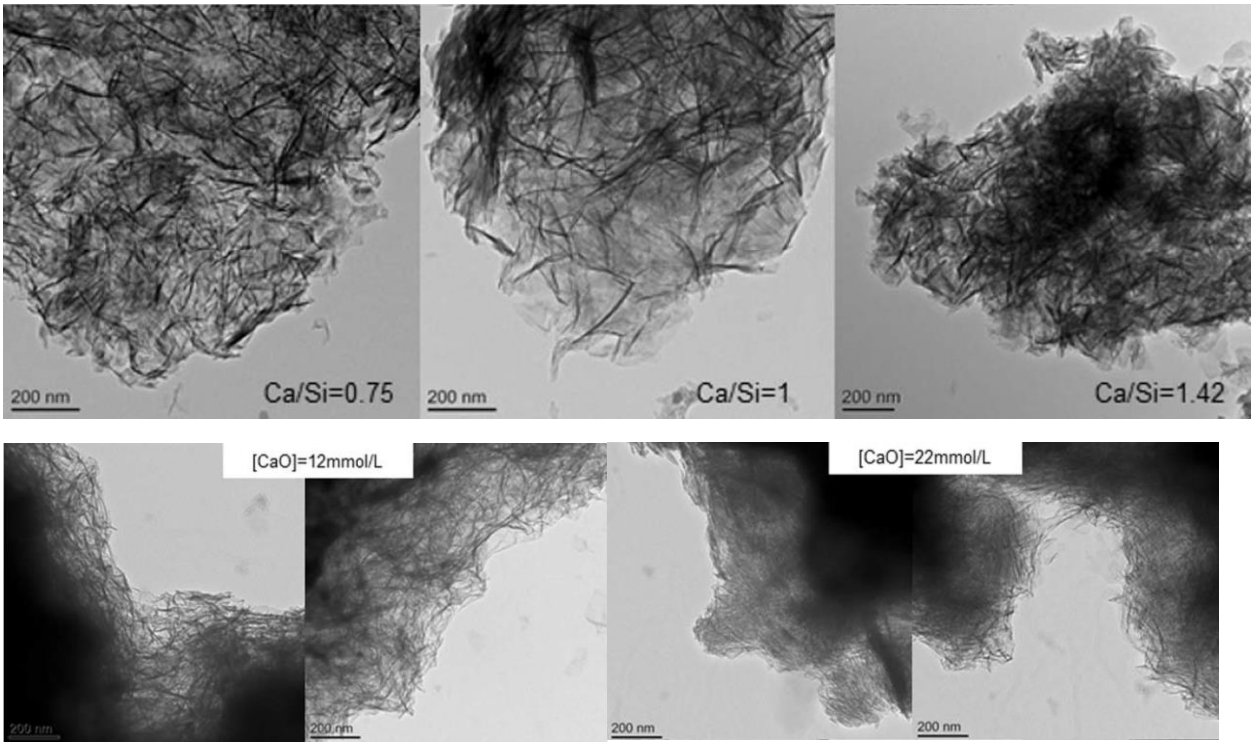

Figure 4 Top row: TEM micrographs of C-S-H with various Ca/Si ratios synthesized by reactions of silica with lime. Bottom row: C-S-H hydrated from tricalcium silicates with different concentrations of CaO [12]

The structure of C-S-H is highly complex; it varies with synthetic methods, Ca/Si ratio, hydration time, and temperature. Nevertheless, understanding the structure of C-S-H is the essential step in controlling its material properties. One strategy to enhance the mechanical properties of concrete is by modifying the layered structure of C-S-H. The following sections will first review some proposed creep mechanisms of concrete and C-S-H, followed by some selected studies on the modifications of C-S-H structure with organic molecules.

1.3 Proposed Creep Mechanisms of C-S-H

There exist different theories and models concerning the creep mechanisms of concrete and C-S-H. Table 1 lists some important theories [13-22].

The creep of cementitious material connects to the viscous nature of C-S-H. Moreover, two creep types can be distinguished: (1) basic creep and (2) drying creep. Basic creep is related to the deformation under constant water content in the material (but not necessarily in a saturated state), while drying creep is related to drying shrinkage under load. The viscoelasticity behavior of cementitious materials is very complex and depends on multiple parameters, such as the age (hydration time) of the sample, temperature history during hydration reactions, age of loading, the intensity of loading, rate of drying, and if drying and deformation occur at the same time [21]. Furthermore, depending on which structural model is used to describe C-S-H, water classification at different length scales could be different.

Jennings proposed one landmark model that concerns C-S-H's structure and creeps relationships. Jennings' CM model emphasizes grain-like C-S-H nanoparticles; within the grain, the structure is a tobermorite-like sheet, and these nanoparticles can cluster together and form globules, which may be viewed as combinations of both colloidal model and layer model (Figure 5 [23]). In addition, although not yet confirmed by the experiment, Jennings suggested the reduced gel porosity under stress due to tighter packing of C-S-H nanoparticles and generation of local stress concentrations and local tighter packing density is linked to concrete creep's initiation process.

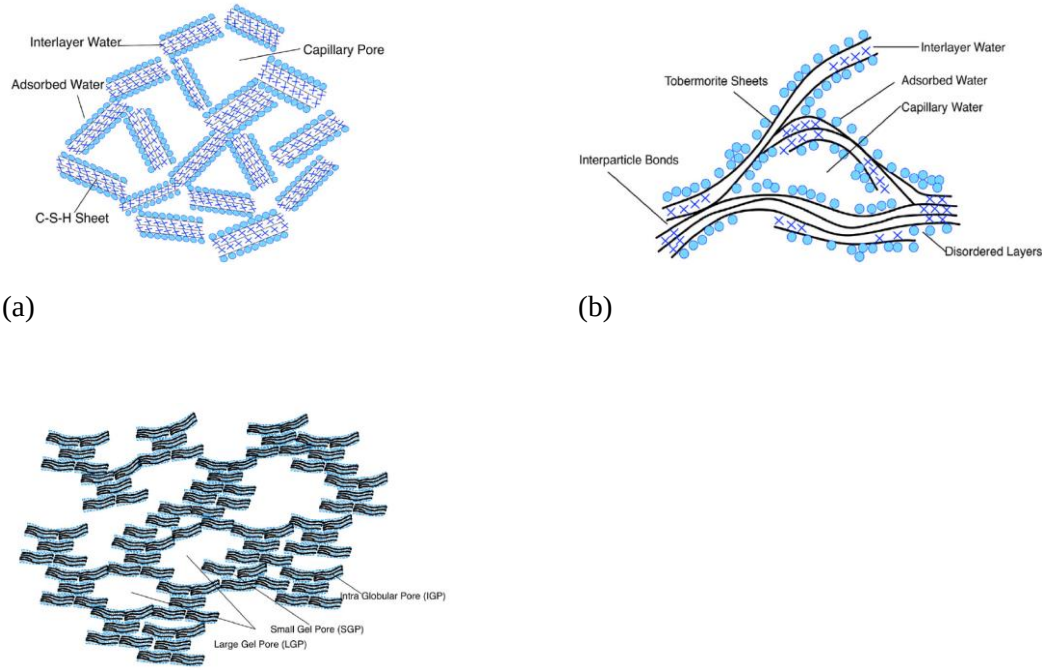

(a) (b)

(c)

Figure 5 Nanostructures of C-S-H (a) Powers and Brownyard model (b) Feldman and Sereda model (c) Jennings model [23]

Bažant: Microprestress-solidification theory

Bažant et al. proposed a microprestress-solidification theory, an improvement of the solidification theory, to account for long-term aging due to the volume growth of the hydration products [16]. Figure 6a illustrates an idealized microstructure of hardened cement paste and shows different water classifications. In this model, long-term creep is believed to originate from viscous shear slips (deviatoric stress) that causes breaking and reforming the interatomic bonds between the two opposite walls of the micropores, as shown in Figure 6b. The microprestress (tensile) is due to chemical volume changes caused by hydration (or drying) and the disjoining pressure (compressive). The entire thickness of adsorption layers is hindered and cannot develop.

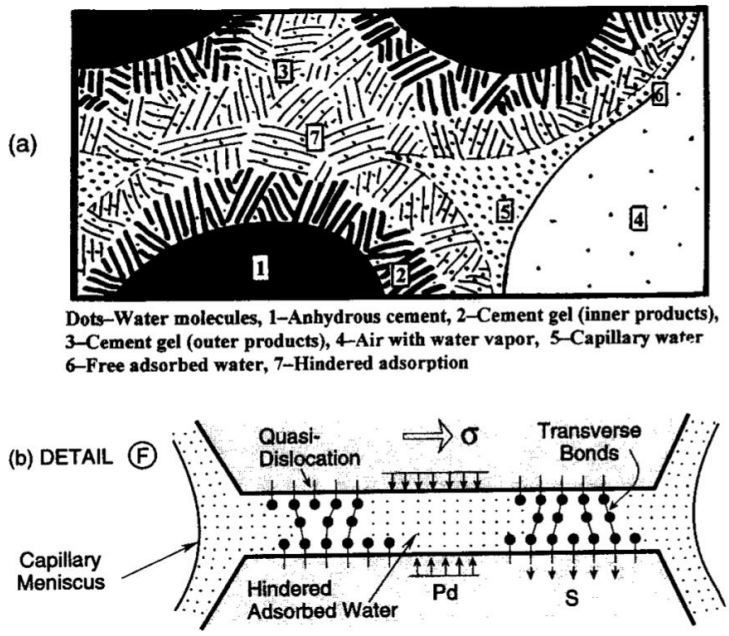

Figure 6 (a) Idealized microstructure of hardened cement paste (b) micropore in cement gel showing disjoining pressure and microprestress [16]

Vandamme and Ulm used the nanoindentation technique and demonstrated that concrete creep could be attributed to the rearrangement of C-S-H nanoparticles. It only depends on the packing density of CSH, shown in Figure 7. Moreover, this rearrangement is consistent with free volume theories of granular media [2]. This study is significant because it indicates that the nanoscale creep measurements in a few minutes by the nanoindentation could predict macroscopic creep over multi-years. However, the nanoindentation technique probes only a small fraction of the sample and may measure localized properties of the sample and does not reveal the bulk material properties.

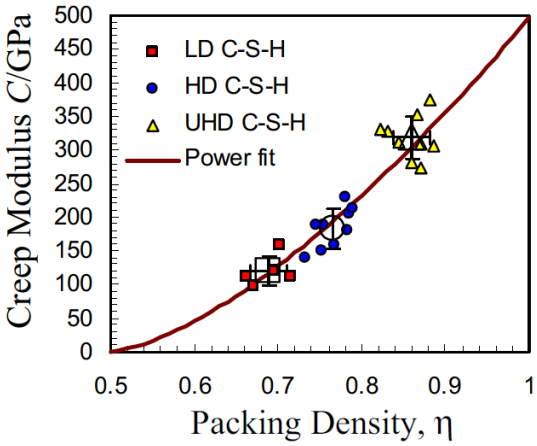

Figure 7 Relationships of creep modulus of CSH and its packing density [2]

In more recent studies, Morshedifard et al. overcome limitations in studying longtime nanoscale phenomena in atomistic simulations by using an incremental stress-marching technique to explore the viscous nature of C-S-H (Figure 8). The simulations, which use a combined logarithmic-exponential function, show that C-S-H exhibits a transition from viscoelastic to logarithmic creep as interlayer water increases [24]. Although their models reaffirm the hypothesis that creep of hydrated cement originates from the reconfiguration of C-S-H particles, the simulations were modeled at the mesoscale and not on the sliding of individual C-S-H sheets.

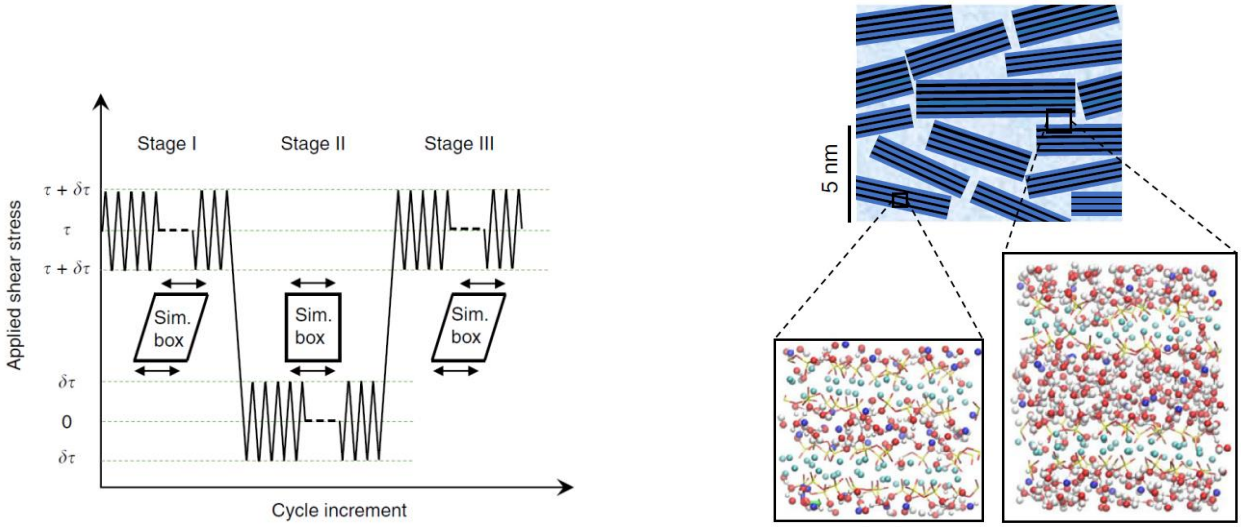

Figure 8 (left) Schematic reforestation of incremental stress-marching cyclic scheme (right) Schematics of C-S-H globules at the mesoscale [24]

Complete mechanisms of concrete creep are still not understood despite numerous research efforts in the past few decades. Nevertheless, researchers widely believe the rearrangement of C-S-H nanoparticles appears to be the root cause of concrete creep based on the available data today. Inspired by these studies, this research applies a high-pressure x-ray diffraction technique to investigate the orientation behavior of C-S-H nanoparticles under deviatoric stresses and successfully showed for the first time, the preferred orientation of C-S-H nanoparticles will begin to occur under deviatoric stresses of around 120 MPa. Results and discussions are provided in Chapter Four. Chapter Five further discusses the high-pressure x-ray diffraction studies on the modified structure of C-S-H nanoparticles and demonstrates promising results for designing more creep-resistant concrete via the bottom-up approach.

Table 1 Different theories for concrete creep [23]

Theory	Remarks	Author
Seepage Theory	Change in the adsorbed water content is a time-dependent seepage process	Powers
Microprestress-Solidification Theory	Long-term creep originates from viscous shear slips (deviatoric stress) that causes breaking and reforming the interatomic bonds	Bažant
Viscous Shear Theory	Adsorbed water acts as a lubricant for slipping C-S-H nanoparticles under shear	Ruetz
Thermal Activation Energy Theory	Thermodynamic forces drive rearrangement of C-S-H; water is not considered explicitly	Wittmann
Rearrangement of Globules	Gel porosity is reduced under stress due to tighter packing of C-S-H; water is not considered explicitly	Jennings
Free Volume Dynamics Theory	Creep of concrete originates from the rearrangement of C-S-H nanoparticles and that it only depends on the packing density of CSH	Vandamme, Ulm
Atomistic Simulations	C-S-H exhibits a transition from viscoelastic to logarithmic creep as interlayer water increases	Morshedifard, Abdolhosseini Qomi

1.4 Modification of C-S-H nanoparticles

The tobermorite-like layered structure of C-S-H is similar to clay, and the strategy to modify polymer/layered silicate (PLS) nanocomposites via intercalations for clay minerals has been widely adopted as it has proven to enhance the resultant materials' mechanical properties remarkably, such as elastic moduli and strength [25, 26]. Three different types of PLS nanocomposites are classified depending on the interactions between the polymer matrix and layered silicate (Figure 9): (1) intercalated nanocomposites, (2) flocculated nanocomposites, and (3) exfoliated nanocomposites.

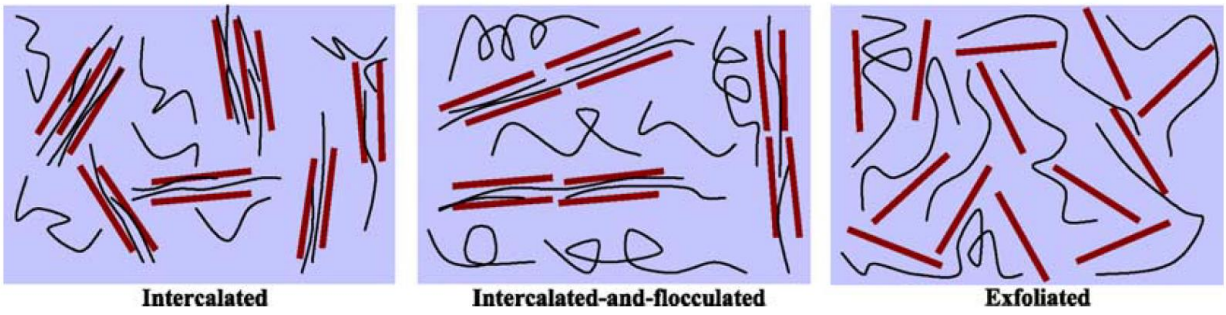

Figure 9 Schematic representations of three different types of polymer/layered silicate nanocomposites [25]

Unlike clay minerals, C-S-H does not have a high swelling capacity and is, therefore, more challenging to intercalate a polymer, with a typical radius of gyration of a few nanometers into the basal spacings of C-S-H, which is only a few angstroms.

Young reported one of the first studies attempting to intercalate nonionic poly (vinyl alcohol) (PVA), anionic poly (acrylic acid) (PAA), and cationic poly(diallyldimethylammonium chloride) (PDC) into the basal spacings of C-S-H [27]. Although the diffraction data capture the shift of the basal peak, showing an increase of the basal spacing due to intercalations, it does not provide other identity diffraction peaks of C-S-H at higher angles. Popova et al. showed contrary results and reported that using a similar type of polymers, the x-ray diffraction and ^{29}Si nuclear magnetic resonance did not show sufficient evidence of structural changes of C-S-H [28]. The topic remains controversial and requires more experimental data to understand the interactions between C-S-H and polymers.

Raki et al. have performed a series of studies on modified polymer C-S-H nanostructures using a variety of characterization techniques, including Fourier-transform infrared photoacoustic spectroscopy, Fourier-transform infrared spectroscopy, x-ray diffractions, x-ray fluorescence, energy dispersed spectroscopy, and ^{29}Si MAS NMR [29-33]. The studies focus on different synthetic strategies and attempt to intercalate various organic contents, ranging from small organic molecules and monomers to polymers with different molecular weights. The data demonstrate promising results of synthesizing C-S-H nanocomposite materials via intercalations. A unique in situ polymerization approach first inserts the monomers into the C-S-H basal spacings, and then the subsequent polymerizations are also demonstrated.

Plank et al. have performed studies on polycarboxylic ether-based (PCE) superplasticizers and C-S-H interactions with PCEs [34-40]. Their works emphasize tailoring molecular structures of PCEs, such as molecular weight and functional groups on the side chains of the polymer. They concluded that PCE does not intercalate into the C-S-H structure as the diffraction experiments did not show a shift of the basal peak. Instead, PCE is entrapped between C-S-H foils, i.e., PCE forms an electrochemical double layer on the surface of C-S-H via ionic interactions between calcium ions and the negative charges on the backbone of the polymers [40]. Contrary to this conclusion, this study adopts a different method to synthesize CSH-PCE nanoparticles and shows that the basal

spacing of the modified CSH-PCE nanoparticles increased from 9.5Å to 13.0 Å, providing strong evidence of intercalation mechanism. Results and discussions are presented in Chapter Three.

1.5 Outline of thesis

Chapter Two provides methods to synthesize C-S-H, CSH-APTES, and CSH-PCE nanocomposites and reviews fundamental theories of x-ray diffraction and the generation of a synchrotron source. The experimental setup of two high-pressure x-ray diffraction techniques, the diamond-anvil cell (DAC) and the D-DIA couples with large volume press, will be presented.

Chapter Three presents DAC measurements of modified C-S-H nanostructures conducted at Lawrence Berkeley National Laboratory (LBNL) and compares the bulk modulus of different modified-CSH materials using x-ray diffraction data. One result indicates that, given sufficient reaction time and the correct pH conditions, the PCEs could intercalate into the basal spacings of C-S-H via silica and lime reactions.

Chapter Four presents the x-ray diffraction results and texture analysis of synthetic C-S-H under shear deformations at Argonne National Laboratory. The challenge and opportunity of using the high-pressure x-ray diffraction technique to study concrete creep will also be discussed.

Chapter Five presents D-DIA measurements of modified C-S-H with organic molecules at Argonne National Laboratory. It explains the development of textures of modified-CSH nanoparticles under deviatoric stresses via an in-situ approach. The results demonstrate that higher deviatoric stresses are required to initiate the texture developments of the intercalated C-S-H nanoparticles, suggesting promising design criteria for making a more creep-resistant concrete.

Finally, Chapter Six concludes this research and proposes some future works to continue the study of concrete creep.

Chapter Two: Materials and Method

2.1 Synthetic C-S-H

While the hydration products of Portland cement typically contains C-S-H with a Ca/Si ratio between 1.7 – 2, this study synthesizes C-S-H samples with bulk Ca/Si ratio of 1.3 to produce phase pure C-S-H materials, as too low of Ca/Si ratio contains unreacted silica, and too high of Ca/Si ratio contains calcium hydroxide.

Calcium oxide (quicklime) was obtained by heating calcium carbonate at 1000 °C for 12 hours via calcination reaction. Stoichiometric amounts of CaO and SiO_2 (Aerosil 200, Evonik) were dissolved in Milli-Q water (Merck Millipore) in high-density polyethylene bottles at the water to solid ratio of 45. The mixtures were stirred with a magnetic bar at room temperature for 182 days. The resultant solid products were filtered with 0.45 μm nylon filters and constantly washed with a 50% v/v ethanol/Milli-Q water (Merck Millipore) solution and ≥94 vol.% ethanol. The filtration process was performed in a vacuum glove box with nitrogen gas to prevent samples from carbonation [41].

2.2 Synthetic CSH-APTES

(3-Aminopropyl)triethoxysilane (APTES) is commonly used in the process of silanization to form strong covalent bonds across the interface between organic and inorganic materials. In concrete technology, researchers use APTES to modify the nanostructure of cementitious materials to improve their mechanical properties. Aminosilanes can act as adhesion promoters, coupling agents, and surface primers [42]. Minet et al. first reported a sol-gel process to intercalate ATPES into C-S-H basal space [43]; Orozco studied CSH-APTES nanocomposites using the HP-XRD technique and showed that the bulk modulus of the modified nanocomposites increases by 38% compared to the phase pure synthetic C-S-H [44]. Moreover, Orozco et al. used XRD, ^{29}Si NMR, synchrotron NEXAFS, and EXAFS in a separate study and showed the silyl functionalities of the PCE-Sil generated covalent bonds through siloxane bridges and increased the silicate polymerization (Figure 10) [45]. More studies on aminosilane with cement-based composites can be found in [46, 47, 48, 49].

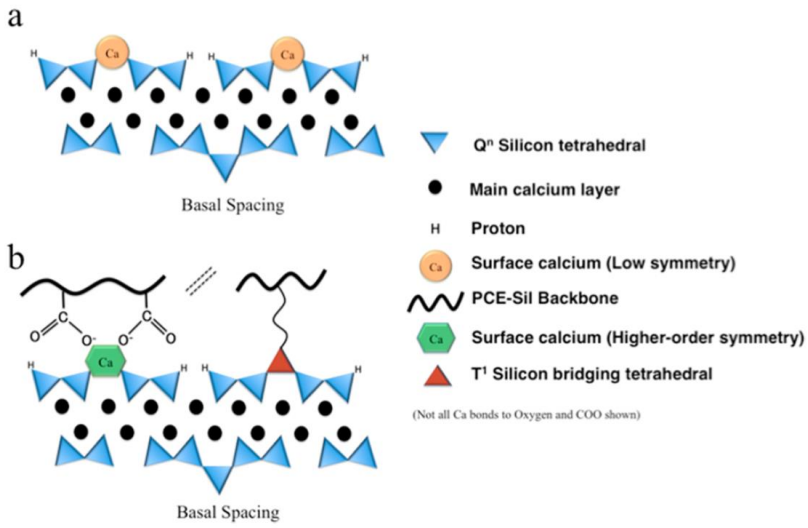

Figure 10 Schematic representation of bonding schemes of (a) phase-pure C-S-H and (b) CSH/PCE-Sil [45]

The CSH-APTES nanocomposites were prepared using similar procedures described in 2.1 and modified based on [44]. First, (3-Aminopropyl)triethoxysilane (APTES, Sigma-Aldrich) with a molar APTES/Si ratio of 1/7 was pre-mixed with Milli-Q water (Merck Millipore). Next, the solution was mixed with stoichiometric amounts of CaO and SiO_2 (Aerosil 200, Evonik) in high-density polyethylene bottles at the water to solid ratio of 45. Finally, the mixtures were stirred at room temperature for 60 days.

A different batch of CSH-APTES nanocomposites was prepared by the coprecipitation method and modified based on [40]. First, stoichiometric amounts of calcium nitrate and sodium silicate were dissolved separately in a small amount of Milli-Q water (Merck Millipore). Both solutions were mixed, and then APTES (Sigma-Aldrich) with a molar APTES/Si ratio of 1/7 were added. The overall water to solid ratio is 45. And the mixtures were stirred at room temperature for two days.

2.3 Synthetic CSH-PCE

The use of natural polymers (e.g., lignosulphonates) as dispersants in concrete dates back to the 1930s. Still, with only about 10% water-reduction ability, its performance is limited compared to synthetic polymers. In the 1960s, the so-called electrostatic dispersants were introduced (e.g., polynaphthalene sulphonates, polymelamine sulphonates, and vinyl copolymers). This category of dispersants' dispersing ability comes from electrostatic repulsions, as the name implies, and the water-reduction capacity ranges from 20 to 30%. A newer generation of comb-shaped polymers, such as polycarboxylate polymers, were developed in the 1980s. This category of dispersants is featured by the long side-chains attached to the polymer backbones and can achieve up to 40% water reduction [50].

When cement reacts with water, the cement particles bearing positive and negative charges interact via favorable electrostatic forces and form flocs (Figure 11). However, if a superplasticizer is introduced into the system, the negative charges along the backbone of the polymers (e.g., COO^-) can be adsorbed onto the surface of positively charged cement particles (or C-S-H) via electrostatic interactions. The dispersion ability then comes from steric repulsions between those polymer side chains attaching to the surface of cement particles (Figure 11); consequently, high fluidity and workability can be achieved [4, 40].

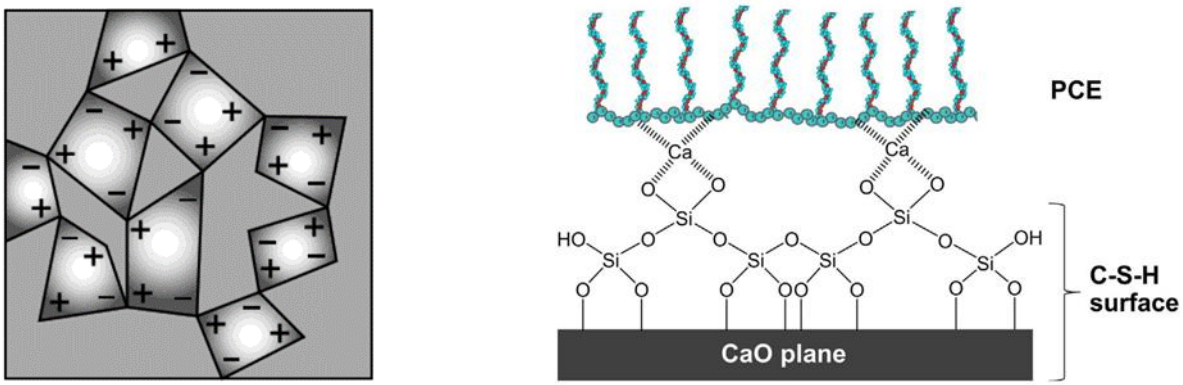

Figure 11 Left: schematic diagram showing cement particles form flocs via electrostatic interactions. Right: PCE with negatively charged backbones adsorbed on a C-S-H surface [4, 40]

PCEs can be synthesized via two approaches: (1) free radical polymerization and (2) esterification (or condensation) reaction (Figure 12). Free radical polymerization is a more cost-effective method to synthesize PCEs and, therefore, more commonly adopted in the industry. However, the resultant polymers generally have higher PDI, i.e., both the molecular weight of polymers and the side chains along the backbone are more randomly distributed, which could negatively affect the performance of the dispersion ability. On the other hand, the condensation reaction yields a narrower PDI and more uniform distribution of side chains along the backbone but often involves more complex chemical reactions.

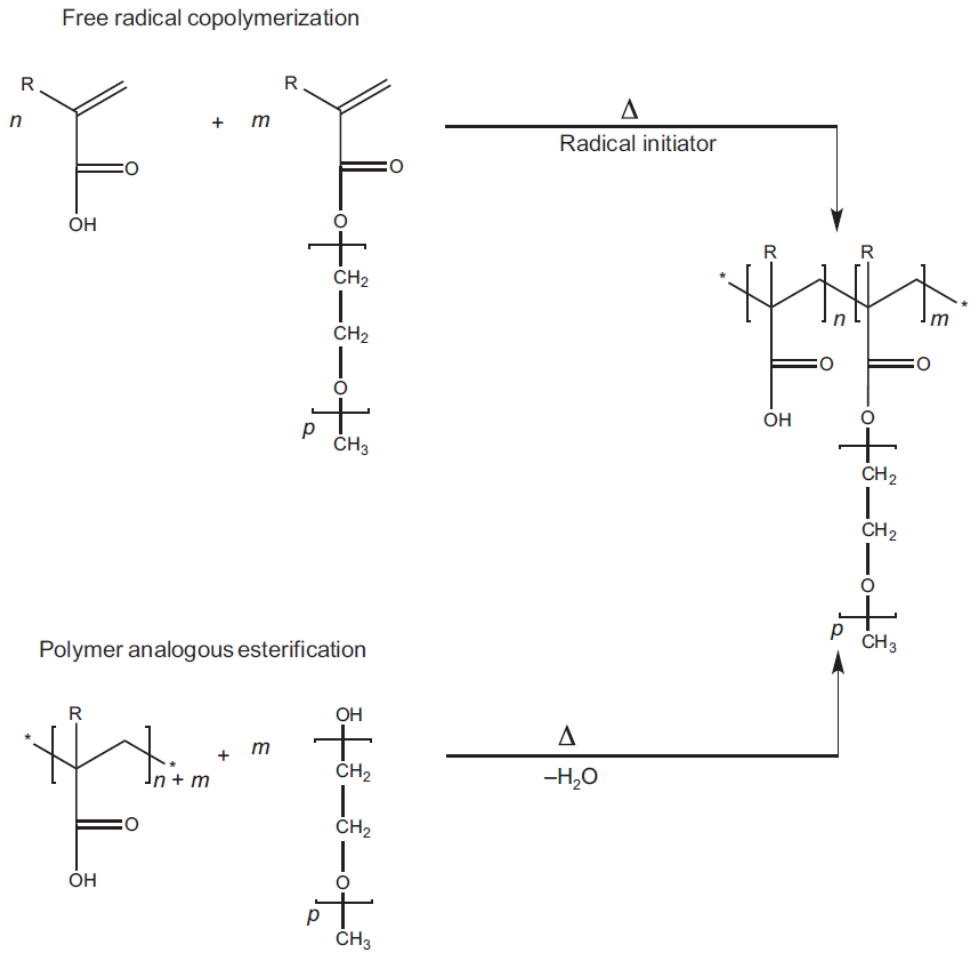

Figure 12 Free radical polymerization and condensation reaction to synthesize PCE [50]

Conformations of comb-shaped polymers in a suitable solvent were proposed by Gay [51]. Depending on the repeating units n, each contains N monomers along the backbone and one side chain of P monomers, five distinct forms of polymers can exist: (1) decorated chain (DC) (2) flexible backbone worm (FBW) (3) stretched backbone worm (SBW) (4) stretched backbone star (SBS) and (5) flexible backbone star (FBS), as shown in Figure 13. For the side chains that are relatively shorter than the backbone, as is the case for most commercially available PCEs, FBW is the dominant form, and the radius of gyration R of the overall chain of FBW polymer in a suitable solvent follows Flory's scaling law:

$$R = (1 - 2\chi)^{1/5} a P^{2/5} N^{1/5} n^{3/5}$$

where
χ = Flory parameter
a = size of monomer
n = number of side chains per core

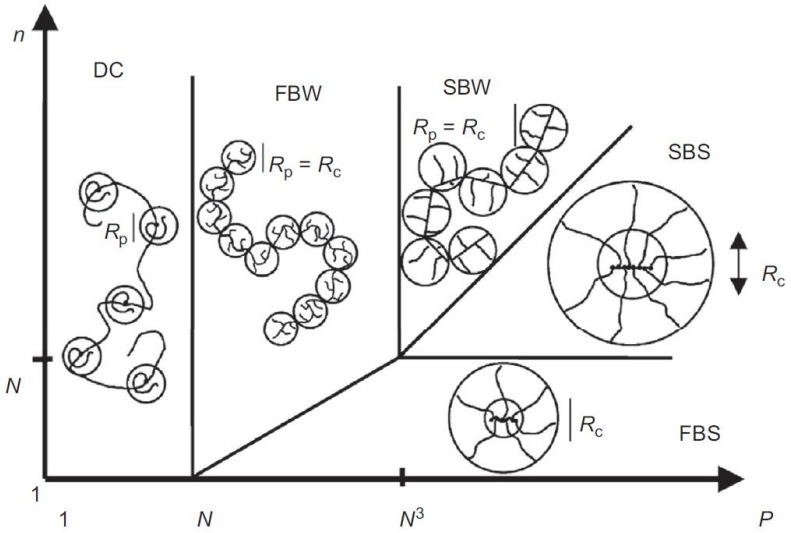

Figure 13 Dependence of conformations on size of backbone/side chain and number of repeating units for comb-shaped polymers [51]

Plank et al. have performed a series of research emphasizing PCE superplasticizers and C-S-H interactions with PCEs [34-40]. Using the coprecipitation method, they found that PCE does not intercalate into the C-S-H basal spacings from XRD experiments. Instead, PCE forms an electrochemical double layer on the surface of C-S-H via ionic interactions between calcium ions and the negative charges on the backbone of the polymers (Figure 11) [40]. Contrary to this conclusion, this study used a different method to synthesize CSH-PCE nanoparticles and apply synchrotron XRD to demonstrate that the basal spacing of the modified C-S-H increases from 9.5Å to 13.0 Å, providing strong evidence of intercalation mechanism.

The CSH-PCE nanocomposites were prepared using similar procedures described in 2.1 and modified based on [40, 44, 52]. First, the pH of diluted PCE solutions was adjusted with NaOH (1 M) to be 13-14. Next, the PCE solution, which contains a solid content of PCE of 3 wt%, was mixed with stoichiometric amounts of CaO and SiO_2 (Aerosil 200, Evonik) in high-density polyethylene bottles at the water to solid ratio of 45. Finally, the mixtures were stirred at room temperature for 60 days.

2.4 X-ray and Synchrotron source

X-rays are electromagnetic radiation with energy ranges from 250 eV to several keV for soft x-ray and from about 10 keV to 100 keV for hard x-ray [53]. X-ray interacts with particles in three different ways: (1) elastic (or Rayleigh) scattering, (2) inelastic (or Compton) scattering, and (3) absorption (or photoelectric effect). These interactions are illustrated in Figure 14 using Bohr's model, and it is the elastic (and coherent) scattering that gives rise to the diffractions. However, this event only accounts for less than ~5 % of the total interactions [54].

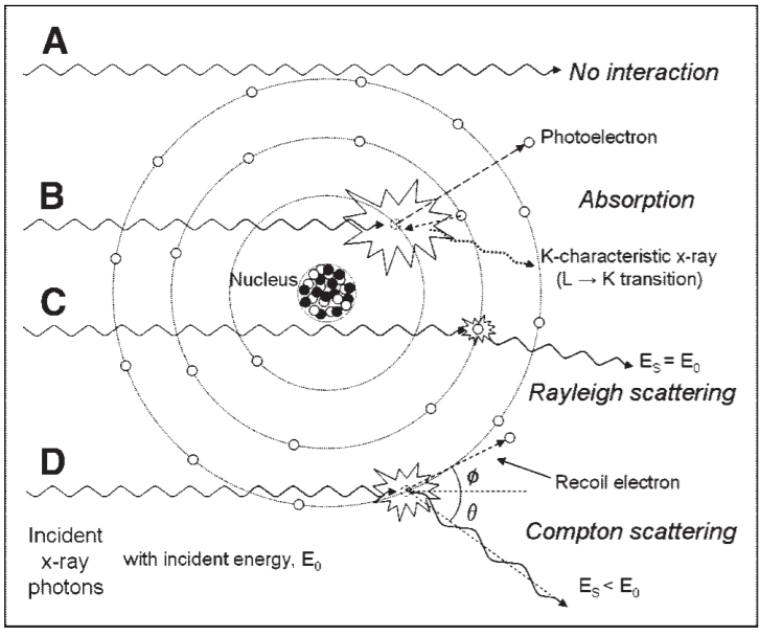

Figure 14 Schematic diagram showing absorption, Rayleigh and Compton scattering [54]

Diffraction arises because of constructive interference between traveling waves, and one of the governing equations in understanding diffraction experiments is Bragg's equation:

$$n\lambda = 2d\sin\theta$$

Where n is an integer, λ is the x-ray wavelength, d is the spacing of the lattice plane hkl, and θ is the angle between incident x-ray and the scattering plane of the sample.

Bragg's analysis is convenient for interpreting the data obtained by diffraction experiments; it serves as the necessary condition for observing diffractions but does not provide reflection conditions (or systematic absences) for a given crystal structure. On the other hand, Laue equations

are more generalized and involve the concept of reciprocal lattice to make connections between diffraction and crystal structure (in the real space). More on the theory of x-ray diffractions can be found in [55, 56].

While x-ray vacuum tubes that generate both bremsstrahlung and characteristic x-rays are used in conventional diffraction experiments, it is often inadequate to examine less crystalline materials or more sophisticated experiments. For example, a typical diffractometer and laboratory x-ray would barely detect the 002 basal peaks for a poorly crystalline C-S-H sample, which is among the most critical piece of information for both texture and intercalation studies. Therefore, at least in this regard, it is highly desired to use synchrotron x-rays for studying less crystalline materials. One reason that synchrotron x-rays can detect weak diffraction peaks of a poorly crystalline material is due to its high brilliance (Figure 15 [57]), which is defined as

$$\text{Brilliance} = \frac{\text{photons/sec}}{(\text{mrad})^2(\text{mm}^2\ \text{source area})(0.1\%\ \text{bandwidth})}$$

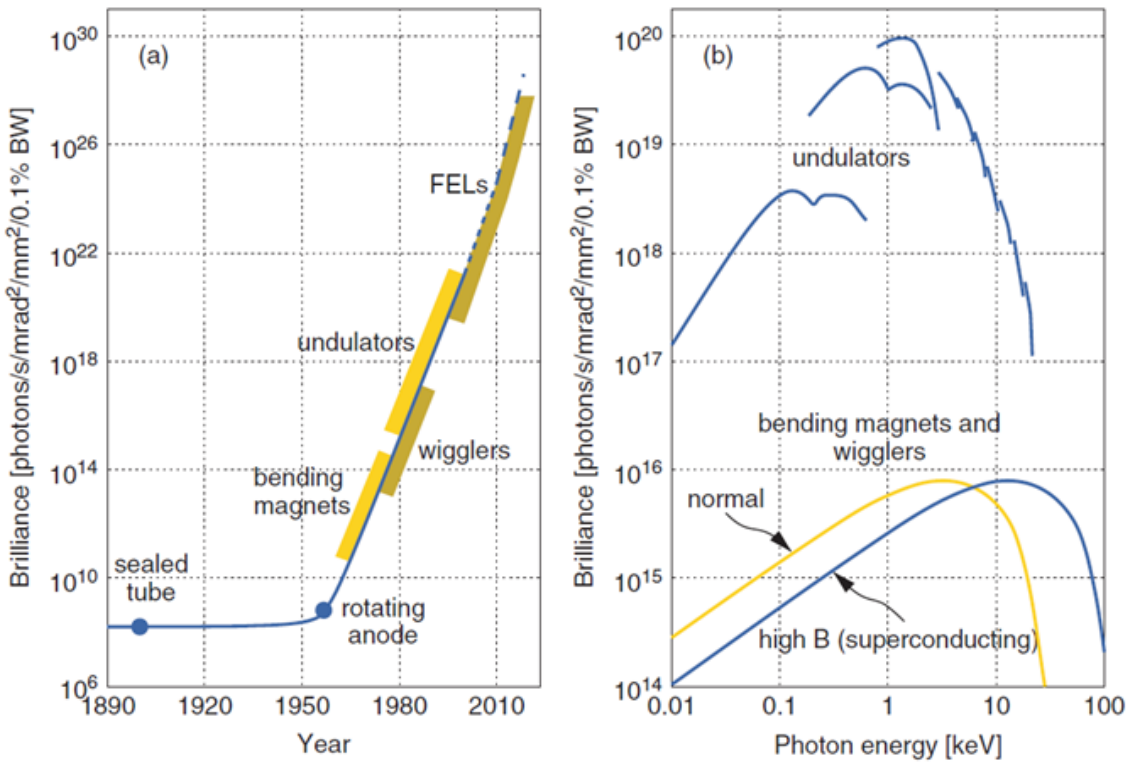

Figure 15 Comparisons of the brilliance of x-ray sources produced by different technologies [57]

Fundamental physics and details of synchrotrons can be found in [53]. In brief, a typical synchrotron facility accelerates electrons with energies ranging from 1-8 GeV at relativistic speed

(nearly the speed of light) in a circulated loop containing bending magnets and insertion devices (Figure 16). Consequently, highly collimated and high brilliance of x-rays is produced, as opposed to isotropic irradiation if the electron travels at velocities much slower than the speed of the light.

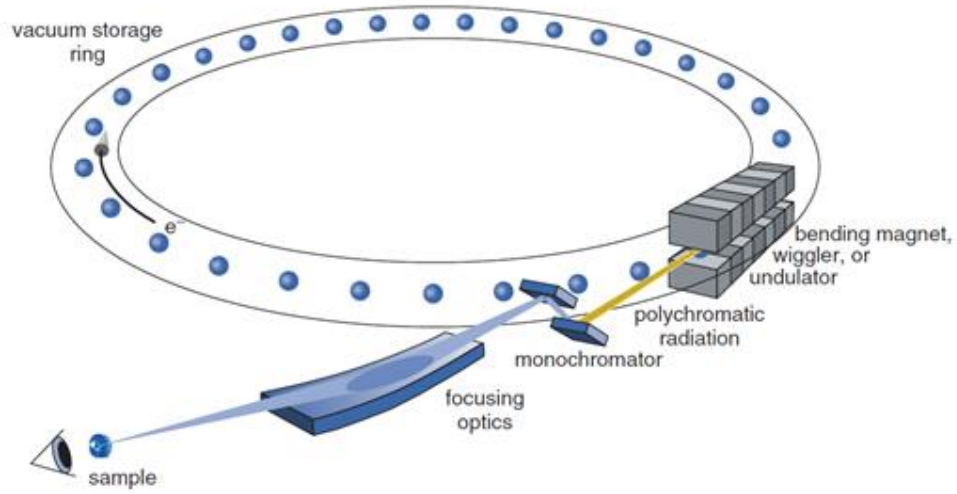

Figure 16 Schematic diagram showing critical components of a third-generation synchrotron [57]

The third-generation synchrotron facility, for example, Advanced Photon Source and European Synchrotron Radiation Facility, is featured by replacing wigglers with undulators and is capable of producing x-rays with minimal angular spread, and hence, achieves brilliance of $\sim 10^{21}$ photons/s/mrad^2/mm^2/0.1% BW, about seven orders of magnitude higher than the first-generation synchrotron using bending magnets, and fourteen orders of magnitude higher in brilliance than a typical laboratory x-ray (Figure 15).

2.5 High-Pressure X-ray Diffraction (HP-XRD)

2.5.1 Diamond Anvil Cell (DAC)

The Monteiro Lab has performed a series of high-pressure experiments on different mineral and cementitious materials using diamond anvil cells (DAC) at beamline 12.2.2. of the Advanced Light Source (ALS) at the Lawrence Berkeley National Laboratory (LBNL) [58-68]. More details on high-pressure experiments using DAC (including experimental setup and texture analysis etc.) can be found in [69, 70].

Figure 17 shows a radial geometry DAC (rDAC), typically chosen to study the texture of the sample material in a high-pressure experiment. By tightening the load screws of the DAC, the pressure is then introduced and applied to the sample. And the change in pressure is measured by the fluorescence signal of the ruby. In this geometry, the diffraction intensities on each Debye ring can immediately show qualitative information about a polycrystalline material's orientations.

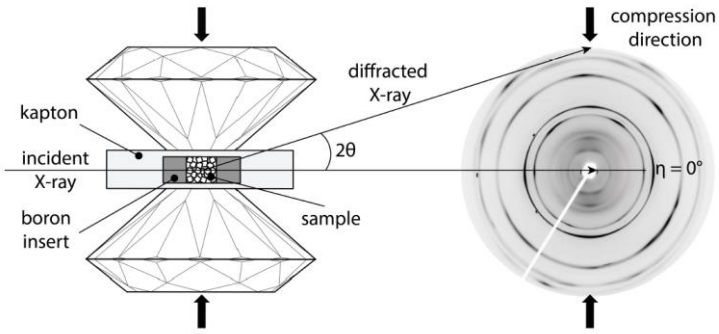

Figure 17 Schematic diagrams showing the DAC and geometry of a typical high-pressure experiment [71]

The Monteiro Lab has confirmed the hypothesis that fiber-like C-(A-)S-H nanoparticles will preferentially orient along the compression axis under uniaxial deformation, and no texture will form under hydrostatic stress using DAC [69]. The work provided new insights into the deformation of C-(A-)S-H, but it has the following limitations: a) the state of the deviatoric stresses in a DAC is complex, and the stress field is not uniform, b) the intensity of the stresses in a DAC is very high, a desirable condition of geophysics research but not realistic in most concrete structures (the compressive strength of a typical normal strength concrete is below 50 MPa [4]), and c) the C-(A-)S-H nanoparticles were prepared at 80 ℃ to increase their crystallinity, but most of the civil infrastructures, such as roads, bridges, and dams are exposed to ambient temperature. Present work addresses all these limitations and, therefore, the results can be incorporated into realistic conditions.

It should be kept in mind that the term "high-pressure" is unfortunately not well defined in the literature and is best to interpret as the conditions that induce some extraordinary effects that cannot be observed under normal (ambient) conditions for the given sample material of study [72].

2.5.2 Large-Volume Press (LVP) System and D-DIA

This study has used the large-volume press (LVP) system and D-DIA at beamline 13-BM-D of the Advanced Photon Source (APS) at Argonne National Laboratory (ANL). D-DIA offers a few

advantages over the DAC. For instance, the system uses a hydraulic press to drive the anvil apparatus and can generate hydrostatic pressure and uniaxial differential stress on the sample separately. Each incremental increase (or decrease) in loads can be controlled in the order of MPa, and strain rate (10^{-3} to 10^{-7} s^{-1}) can also be programmed and measured by x-ray radiography. Moreover, with sample volumes of about 10^3 to 10^6 times larger than DAC, a better statistic can be obtained. Lastly, although not relevant to the present work, the system can generate more uniform pressure-temperature conditions, vital for geoscience applications [72].

LVP systems for synchrotron typically consist of the followings: (1) a hydraulic press with a load control system, (2) a set of guild blocks (pressure module), (3) an electrical heating system to control temperature (4) x-ray optical components for diffraction and imaging (5) x-ray and image detectors and (6) a goniometer. The D-DIA, which uses tungsten carbide anvils (see Figure 19), was described in detail in [72, 73]. The modified DIA apparatus has the feature to independently control additional pairs of anvils driven by the differential rams. Figure 18 illustrates the experimental setup with D-DIA deformation apparatus at beamline 13-BM-D at APS [74].

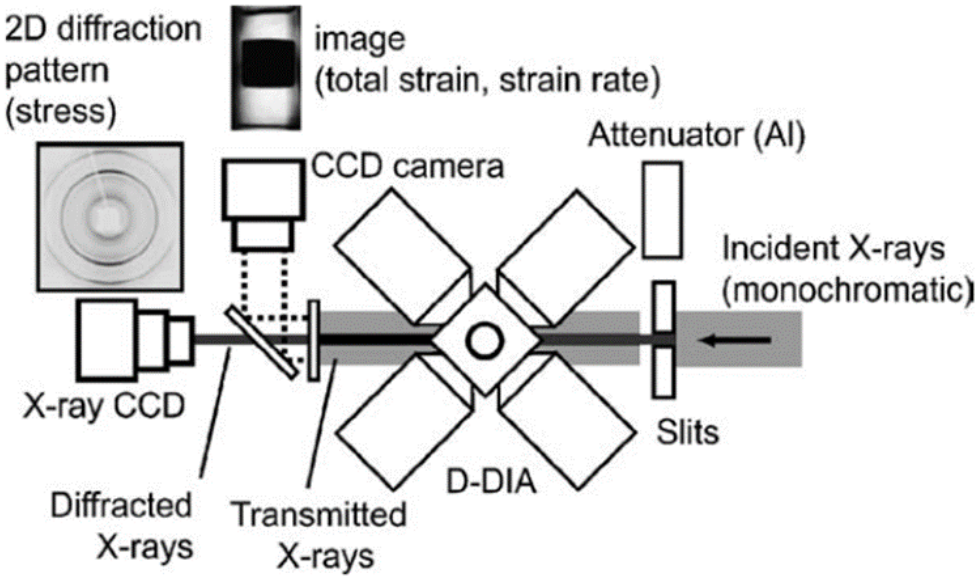

Figure 18 Schematic diagram showing the experimental setup with D-DIA deformation apparatus [74]

Figure 19 shows the geometry of the D-DIA high-pressure experiment, where synchrotron x-rays penetrate through the sample, and the area detector, which is perpendicular to the direction of the incoming x-ray, records the diffraction patterns (Debye rings). See more discussions of the experimental setup in the texture analysis section.

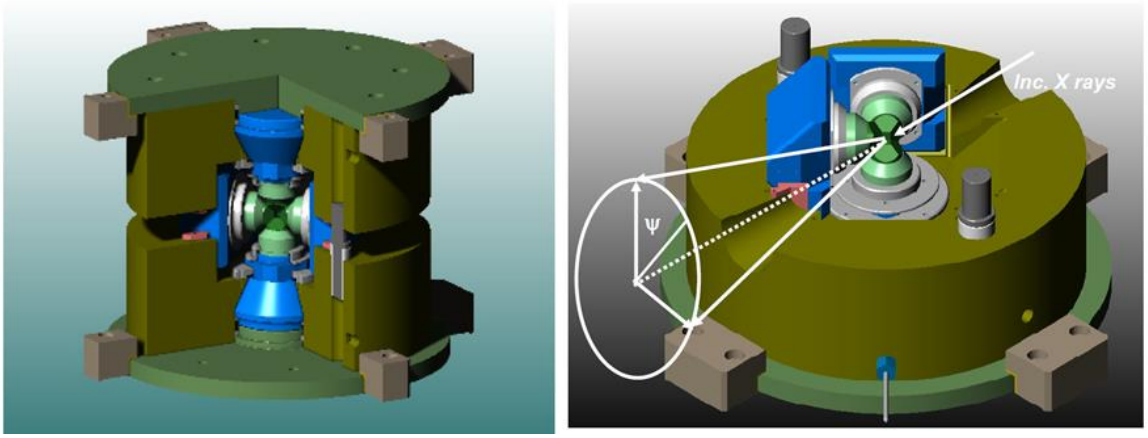

Figure 19 Schematic diagram showing D-DIA cubic anvil apparatus [72]. Ψ is the angle along the Debye ring

One significant advantage of this geometry is that if the crystallites of a polycrystalline material in the sample powder are randomly oriented, the diffraction intensities on each Debye ring would appear continuous since it is equally likely for the crystallites to orient in any direction. On the other hand, if the crystallites are preferentially oriented in specific directions – for example, due to material processing, then diffraction intensities on the Debye ring would not be homogeneous; instead, higher diffraction intensities would be expected at some angles Ψ. By analyzing the relevant diffraction peak as a function of Ψ (in C-S-H, the relevant peak is 002), one can then quantify the strength of texture using pole figures or inverse-pole figures.

The pressure medium to hold the sample material and be used in the LVP is a solid cube with dimensions of 12×12×12 mm^3; at the cube center, a cylindrical capsule with a 4 mm diameter is drilled for loading the sample material. The sample length is restricted by the area that the camera can capture and is approximately 5 mm. Furthermore, C-S-H powder samples were loaded directly into the sample holder (pressure medium) without forming a pellet to avoid inducing texture during sample loading.

In the sample holder, densified and crushable alumina was placed on both ends of the sample to serve as pistons. It was also used for instrument calibrations, for example, to calculate sample to detector distance based on the fitting of measured diffraction patterns with corundum CIF.

Two thin gold foils were also placed on both ends of the sample. During deformations, the macroscopic axial strain of the sample was measured by the fluorescence signals from the gold foils using x-ray radiography.

Since specifications and processing conditions of all pressure medium materials being used are not available, the potential anisotropic behavior arising from the pressure medium materials has been neglected.

The x-ray energy was 50 keV (0.248Å), and a Mar165 charge-coupled device (CCD) was used to record the diffraction patterns with the exposure time of 500 seconds. The sample was first

compressed quasi-hydrostatically to 5 tons (30 MPa), followed by uniaxial compression with the differential rams at the strain rate between 0.003%-0.005% per second. Similar procedures were repeated for all C-S-H samples being investigated in this study.

2.6 Texture Analysis

2.6.1 Texture Analysis with Synchrotron X-ray

Until (fast) area detectors for synchrotron were implemented, texture analysis had been a relatively slow process. Depending on the methods of experiments to collect diffractions, the analysis often involves complex theories and computations. Wenk and others were the first to utilize synchrotron x-rays couples with area detectors and demonstrated that the process of texture analysis could be expedited [75-79]. A typical texture analysis process can be summarized in a flow chart, as shown in Figure 20.

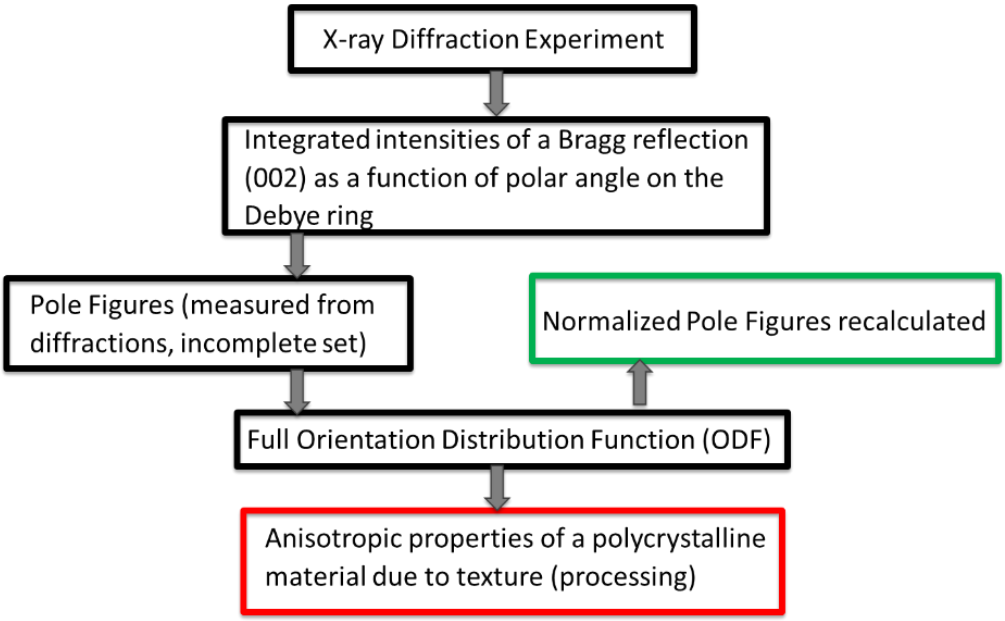

Figure 20 A general process for texture analysis from an X-ray diffraction experiment

The key advantages of using synchrotron x-rays for texture study include: (1) better angular resolution, (2) faster data collection, and (3) allows transmission geometry. Rapid data collection makes it possible to probe deformation in situ under high-pressure experiments, i.e., direct observation of phase transformation of the material in real-time is possible.

There exist different experimental setups to perform texture analysis with x-ray diffractions. And one of the simplest methods for analyzing a polycrystalline material with monochromatic x-ray (single wavelength) is by placing a two-dimensional detector perpendicular to the direction of the incident x-ray that transmits through the sample (Figure 21 [71]). The Ewald sphere, reciprocal lattice vector, and diffraction center (for a hkl plane) then define a diffraction cone, and the "ring" gets recorded on the detector is referred to as the Debye ring. This experimental geometry will be used throughout the study.

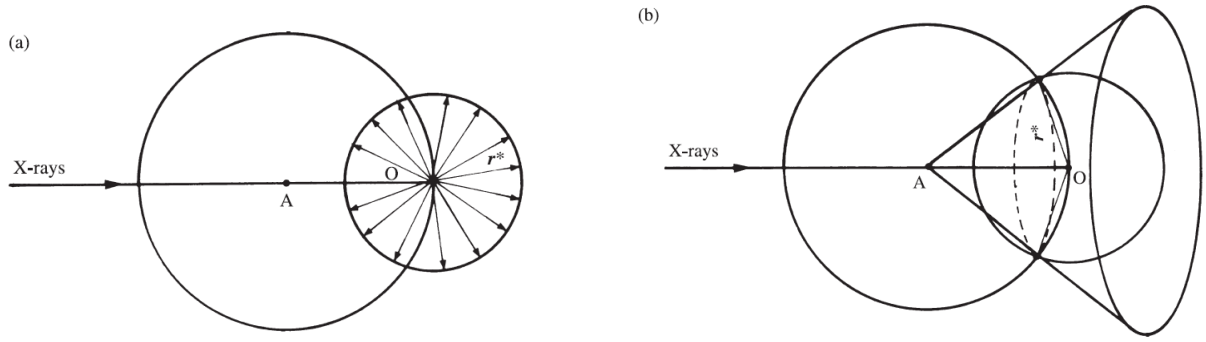

Figure 21 (a) scattering center (A) in Ewald sphere with corresponding reciprocal lattice vector r^* for randomly oriented crystallites. (b) a Debye ring constructed from an Ewald sphere, r^* and a scattering center [71]

2.6.2 March-Dollase Function

Jeffery published one of the earliest theoretical works on studying the dynamic orientation of rigid particles in a viscous matrix in 1923 [80], later, static orientation distribution (or development of preferred orientation) as a result of the rigid-body rotation of platy or rod-shaped grains upon linear deformation was published by March in 1932 [81]. In 1986, Dollase introduced a mathematical function based on March's function, later known as the March-Dollase model, for correcting diffraction intensities due to preferred orientation in powder diffractometry [82].

March-Dollase function is widely used and has the form

$$P(\eta) = \left(r^2\cos^2\eta + \frac{1}{r}\sin^2\eta\right)^{-3/2}$$

where r is called the March parameter (a refinement parameter), η is the tile angle of [002] from the compression axis. The goal of a typical refinement process is to adjust r (along with other

refinement parameters) until calculated diffraction intensities agree well with observed diffractions. The overall expression for the calculated intensity is given by

$$I = sLP(\alpha)F^2$$

where s is the scale factor; L is combined Lorentz polarization; F is structure factor

March parameter characterizes the strength of preferred orientation; the two extreme cases are (1) $r = 1$, which indicates random orientation, and (2) $r \to 0$, which implies perfect preferred orientation.

Numerous models exist in the literature for describing pole-density, but there are several advantages of utilizing the March function:

(1) March function is a true probability distribution function. The function is smooth and symmetric and gives unit integral

(2) March function has a valid theoretical basis and is related to major mechanisms that produce preferred orientation

(3) The same functional form can be applied to both platy and elongated shape crystallites

(4) The function contains a single variable r for refinements

2.6.3 Pole Figures

We use pole figures to quantify textures from the recorded diffraction images, where the lattice plane orientation distribution is described in the frame of the sample space, e.g., in metallurgy, the three sample axes are typically defined as the rolling direction (RD), the transverse direction (TD), and the normal direction (ND) (Figure 22) [83]. A pole figure is the 3-dimensional representation of poles to lattice planes on a sphere. This sphere is then projected onto a plane. Figure 23 shows an example of a 100 pole figure where the crystallites are oriented to align with the axes defined by the rolling, transverse, and normal directions [84].

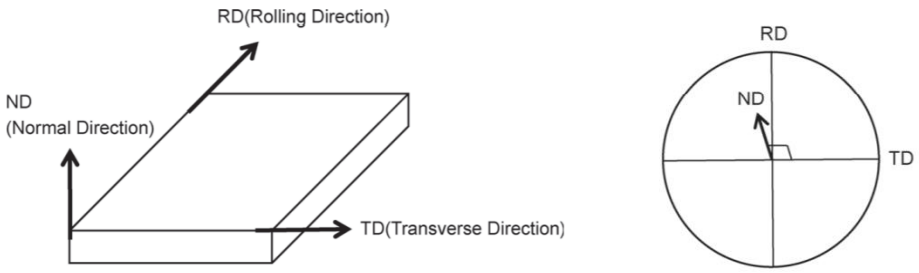

Figure 22 Left: Definition of RD, TD, and ND in a sample's space. Right: Definition of RD, TD, and ND in pole figure [83]

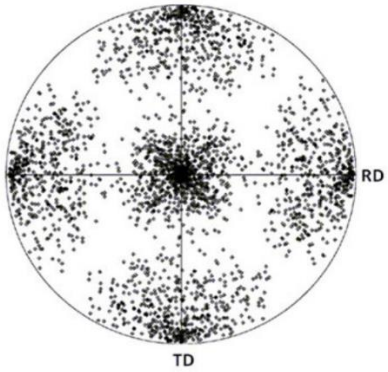

Figure 23 A 100 pole figure indicating cube texture, i.e., the (100) planes are perpendicular to the normal direction [84]

For a polycrystalline material with many grains, poles may overlap too much, and that the details of the true orientation density may be lost. In light of this, contour lines separate areas with different pole intensities are used instead, and the multiple of random distribution (m.r.d) value represents the statistical values or the degree of preferred orientations of the sample. Figure 24 shows a C-S-H sample that forms preferred orientations under deviatoric loads. Moreover, in Chapter Three and Chapter Four, HP-XRD results of DAC and D-DIA confirm that hydrostatic pressure does not introduce texture. Only shear stress (deviatoric stress) can induce the texture formation of C-S-H nanoparticles.

The pole figures in this study are presented in that the compression direction is perpendicular to the center of the pole figure. The differential stress causing the observed strain is defined as $t = \sigma_{33} - \sigma_{11}$, where σ_{33} is the compressive stres. And due to the assumption of axial symmetry, $\sigma_{11} = \sigma_{22}$. More discussions on texture analysis of C-S-H under shear stresses are presented in Chapter Four and Chapter Five.

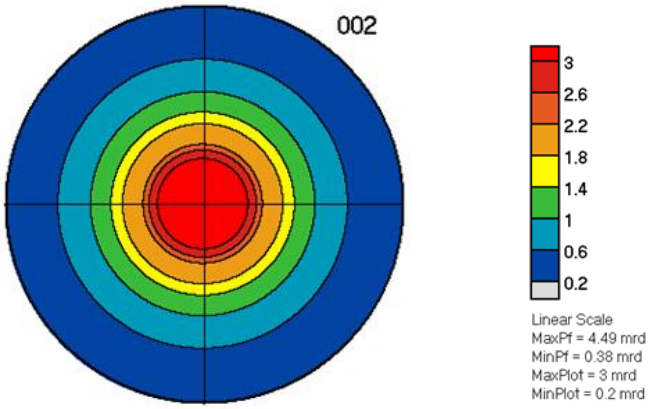

Figure 24 A pole figure of a C-S-H sample showing strong texture under shear loadings

Chapter Three: The Structure and Property Relationships of Modified-CSH Nanocomposites

3.1 CSH-PCE Nanocomposite

The deformation experiment on CSH-PCE nanocomposites was performed at beamline 12.2.2 of the ALS. The experiment used a diamond anvil cell in radial geometry (rDAC) (see 2.5.1 for more details on DAC). A monochromatic x-ray of spot size of 10 μm with an energy of 20 keV (or 0.62 Å) was used for the diffraction. The diffraction images were recorded with a PILATUS detector, and the x-ray exposure time was 360 seconds. The fluorescence signal from a ruby measured the pressure applied to the sample during deformation.

Figure 25 shows some selected DAC measurements of the CSH-PCE sample under three different hydrostatic pressures. Complete data are available in the appendix. Table 2 summarizes the basal spacings and the bulk modulus of various modified C-S-H samples.

In contrast to the phase pure C-S-H sample, the 002 basal peak of the CSH-PCE sample increases from 9.5 Å to 13.0 Å, indicating that the expansion of the basal spacing could be due to intercalation of PCEs. However, an increase by only a few Å implies "partial intercalation" of the polymers. Considering the electrostatic effect, the neutral charges side chains rather than negatively charged backbones will likely be inserted into the basal space. The results suggest that the kinetics of the chemical reactions could significantly affect the intercalation mechanism; unlike the coprecipitation method used by Plank [40], where the C-S-H product typically forms in 1-3 days, the chemical reaction of dissolving lime and silica to form C-S-H takes 28 days or longer. The much slower kinetics may be the reason for allowing the arrangements of the resultant CSH-PCE nanostructure.

However, this structural modification appears to be chemically unstable even at room temperature. Figure 26 shows the diffraction of the same CSH-PCE sample taken after being stored in a vacuum for about a year at room temperature. The 002 peak of this aged sample becomes too broad, and the full peak could not be measured. Although the translational motion of the entire PCE molecule requires higher thermal activation energy (above the glass transition temperature of the polymer), given sufficient time, the disruption of the arrangements that cause the broader 002 peak could be due to the movements of "cooperative wriggling" along the side chains of the polymers, where the entropic effect outpace the enthalpic stabilization.

These results provide hints of designing hybrid-CSH nanocomposite materials and highlight the complexity of the material. Moreover, if the modified structure evolves, the corresponding mechanical properties may also be sensitive to a time dependency.

The bulk modulus of the CSH-PCE sample is determined by measuring the pressure-induced volumetric change and using the third-order Birch-Murnaghan equation of state (BM-EoS) [85]:

$$P = \frac{3}{2}K_0\left[\left(\frac{V}{V_0}\right)^{-\frac{7}{3}} - \left(\frac{V}{V_0}\right)^{-\frac{5}{3}}\right]\left[1 + \frac{3}{4}(K_0' - 4)\left(\left(\frac{V}{V_0}\right)^{-\frac{2}{3}} - 1\right)\right]$$

where P is the pressure, V_0 is the initial unit cell volume at ambient pressure, V is the volume of the unit cell at pressure P, K_0 and K_0' are the bulk modulus and its pressure derivative, both at ambient state. If K_0' for zeolites is assumed a constant value of 4 [86, 87, 88], the above equation is simplified to:

$$P = \frac{3}{2}K_0\left[\left(\frac{V}{V_0}\right)^{-\frac{7}{3}} - \left(\frac{V}{V_0}\right)^{-\frac{5}{3}}\right]$$

Figure 27 shows the fittings of the pressure-volume relationship of the CSH-PCE sample with BM-EoS, the band within the trend line indicates the confident prediction zone. The computed bulk modulus of the CSH-PCE sample is 42.8 ± 2.8 GPa, roughly the same value as the phase pure C-S-H sample [44], indicating the polymers are "loosely packed" and do not give superior enhancement of material's mechanical properties as compared to some of the reported PLS nanocomposites [25, 26].

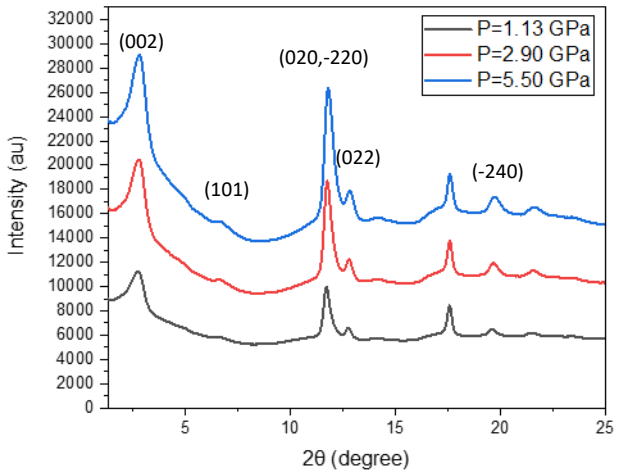

Figure 25 Selected DAC measurements of the CSH-PCE sample at different hydrostatic pressures

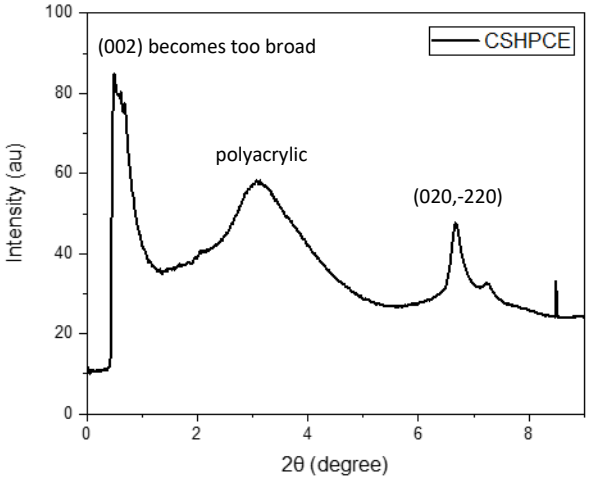

Figure 26 Diffraction measurement of the CSH-PCE sample after the samples being stored in a vacuum for about a year at room temperature

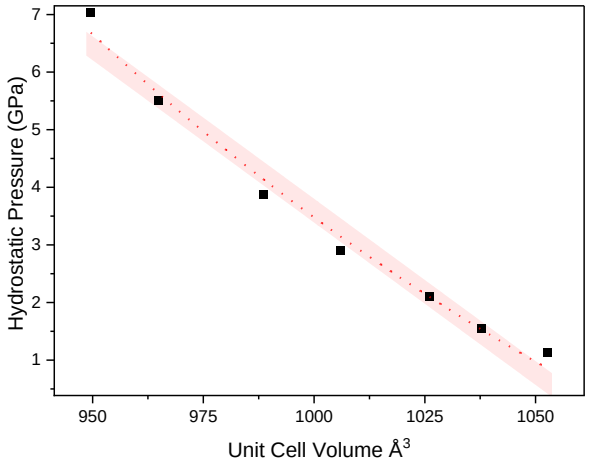

Figure 27 Fittings of the pressure-volume relationship of CSH-PCE sample with Birch-Murnaghan equation of state

3.2 CSH-APTES Nanocomposite

The mechanical properties of CSH-APTES nanocomposites synthesized with lime and silica have been studied using DAC [44]. In this study, the same CSH-APTES sample (labeled as **CSH-APTES A**) was reproduced and investigated again with DAC for reference purposes; another batch of CSH-APTES samples was synthesized using the coprecipitation method (labeled as **CSH-APTES B**).

The deformation experiments on both CSH-APTES nanocomposites were performed at beamline 12.2.2 of the ALS. The experiment used a diamond anvil cell in radial geometry (rDAC) (see 2.5.1 for more details on DAC). For CSH-APTES A, a monochromatic x-ray of spot size of 10 μm with an energy of 20 keV (or 0.62 Å) was used for the diffraction. The diffraction images were recorded with a PILATUS detector, and the x-ray exposure time was 360 seconds. For CSH-APTES B, a monochromatic x-ray of spot size of 10 μm with an energy of 25 keV (or 0.496 Å) was used for the diffraction. The diffraction images were recorded with a MAR 345 detector, and the x-ray exposure time was 900 seconds. The fluorescence signal from a ruby measured the hydrostatic pressure applied to the samples during both experiments.

Figure 28 shows some selected DAC measurements of the CSH-APTES A sample under three different hydrostatic pressures. Complete data are available in the appendix. The 002 basal peak of the CSH-APTES A sample increases from 9.5 Å to 12.5 Å, slightly more than previous studies [44], and confirms the intercalation of APTES molecules.

This structural modification also changes over time. Figure 29 shows the diffraction of the same CSH-APTES A sample taken after being stored in a vacuum for about a year at room temperature. In contrast to the CSH-PCE sample, the 002 peak of this aged CSH-APTES A sample becomes

sharp and intense, while the basal spacing remains similar (a slight increase from 12.5 Å to 13 Å). These results suggest the CSH-APTES A sample is relatively more stable, and the material has increased crystallinity along the c-axis over time (i.e., more ordering of the 002 planes). Unlike the CSH-PCE sample, where the polymer arrangements are seemingly driven by entropic effect, the arrangement of APTES molecules within the C-S-H basal space appears to be dominated by enthalpic forces.

Figure 31 shows some selected DAC measurements of the CSH-APTES B sample. The 002 basal peak of this modified sample increases from 9.5 Å to 17.3 Å. The results suggest that the kinetics of the chemical reactions could significantly affect the intercalation mechanism. One possible explanation is that the much faster coprecipitation reaction initially allows many APTES molecules to intercalate into the C-S-H basal spacing without much ordering. Therefore, a broad and much larger basal peak is observed. However, Figure 32 also shows that this structural modification evolves. The 002 peak of this aged CSH-APTES B sample becomes sharp and intense. At the same time, the basal spacing decreases significantly from 17.3 Å to 14.6 Å, indicating the material again has increased crystallinity along the c-axis, and some initially intercalated APTES molecules are possibly "disposed of away" from the basal spacings. These results support the hypothesis that enthalpic forces outpace the entropic effect for CSH-APTES nanocomposites.

Figure 30 and Figure 33 show the fittings of the pressure-volume relationship of the CSH-APTES A and CSH-APTES B samples, respectively, using BM-EoS. The computed bulk modulus of the CSH-APTES A sample is 74.9 ± 3.9 GPa, a 66% increase compared to the phase pure CSH material [44]. The bulk modulus of the CSH-APTES B sample is 72.2 ± 1.4 GPa. The slightly higher value of the modulus of CSH-APTES A sample may imply that the slower forming CSH-APTES product from the lime and silica reactions could produce a more chemically stable and tighter-packed structure. However, it requires further investigations to verify this observation as the two values are too similar, considering the experimental errors. More insight and the studies on behaviors of the preferred orientations of both samples under deviatoric stresses are presented in Chapter Five.

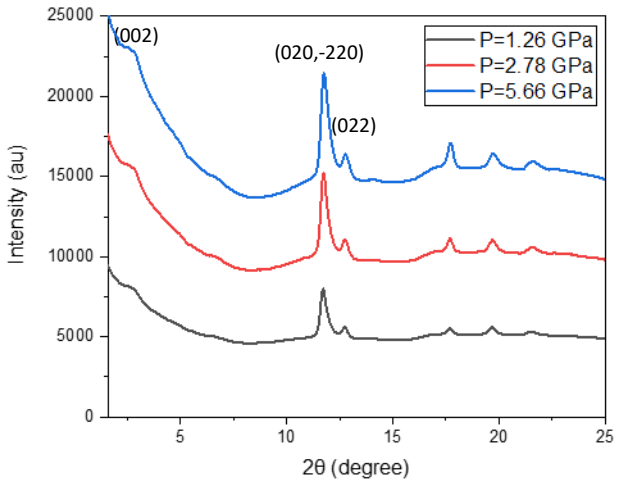

Figure 28 Selected DAC measurements of the CSH-APTES A sample at different hydrostatic pressures

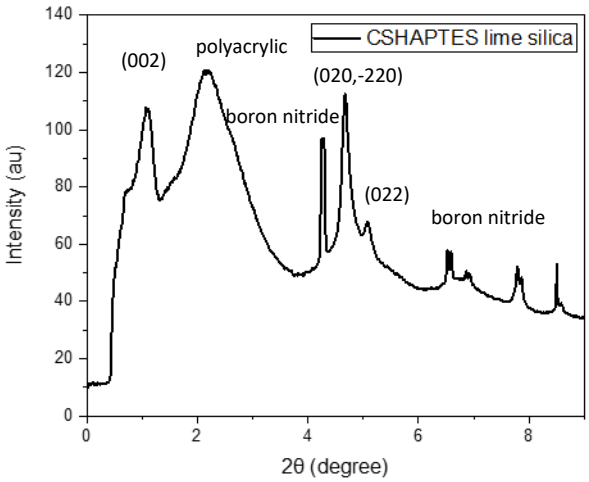

Figure 29 Diffraction measurement of the CSH-APTES A sample after the samples being stored in a vacuum for about a year at room temperature

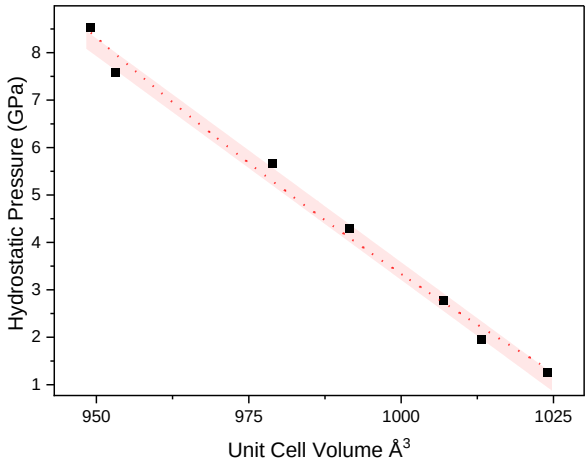

Figure 30 Fittings of the pressure-volume relationship of CSH-APTES A sample with Birch-Murnaghan equation of state

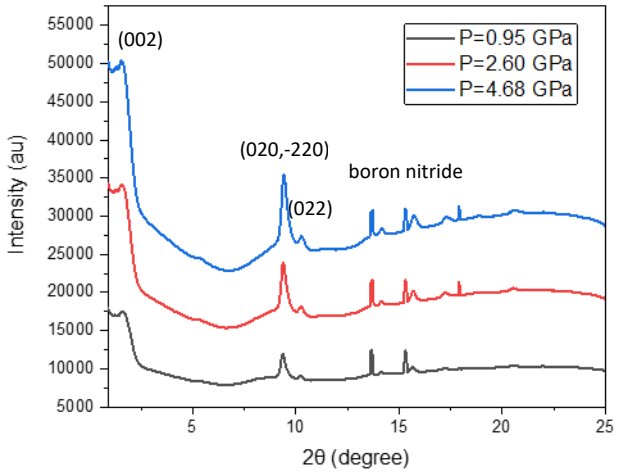

Figure 31 Selected DAC measurements of the CSH-APTES B sample at different hydrostatic pressures

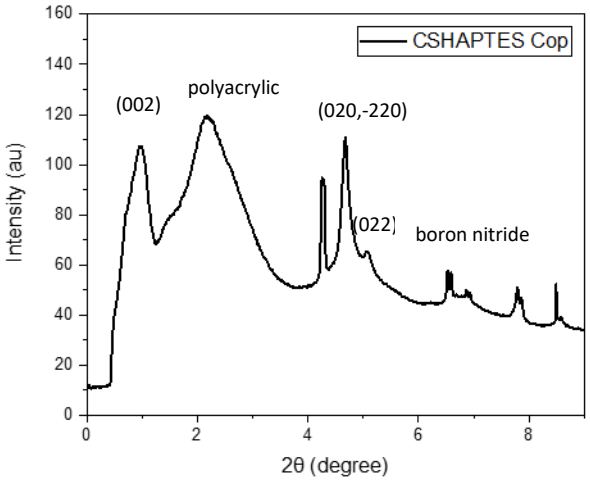

Figure 32 Diffraction measurement of the CSH-APTES B sample after the samples being stored in a vacuum for about a year at room temperature

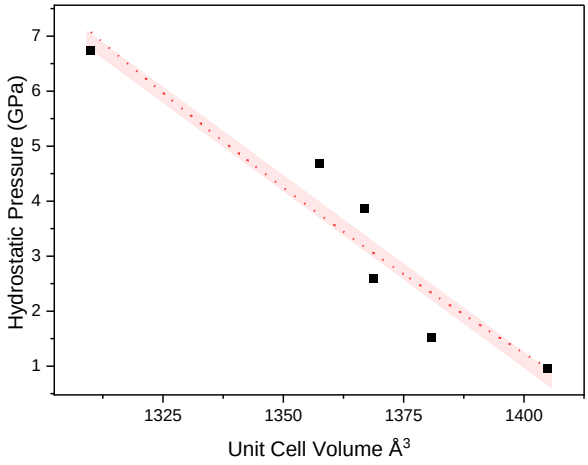

Figure 33 Fittings of the pressure-volume relationship of CSH-APTES B sample with Birch-Murnaghan equation of state

Table 2 Summary of basal spacings and bulk modulus of different modified CSH samples

	Basal spacing Å	Bulk modulus GPa
C-S-H	9.5	45.0 ± 3.0
CSH-APTES A	12.5 (to 13.0 after 1 year)	74.9 ± 3.9
CSH-APTES B	17.3 (to 14.6 after 1 year)	72.2 ± 1.4
CSH-PCE	13.0	42.8 ± 2.8

Chapter Four: Shear Deformations of C-S-H

4.1 Cyclic Loading Experiment on C-S-H

The HP-XRD experiments were conducted at the beamline 13-BM-D at APS, and the experimental setup and conditions are described in Chapter Two. One unique feature at the beamline 13-BM-D is that cyclic loadings in compression to deform the sample material can be programmed. Figure 34 shows the stress and strain results of the cyclic loadings experiment on C-S-H, and illustrates an apparent viscoelastic behavior of the material, which researchers widely agree is connected to concrete creep.

We compressed the sample hydrostatically to about 30 MPa and further strained the sample to about 5-6% to ensure the powder sample was tightly packed. The speed of the differential rams constrains the loading period (frequency) and amplitude.

The computed storage modulus from Figure 35 and Figure 36 was 309.6 MPa; the pores present in the sample volume space most likely contributed to the low stiffness value. Nevertheless, the results successfully demonstrate that HP-XRD is a powerful technique to investigate cementitious materials' highly complex viscoelastic behavior. To our knowledge, it also provides the first available data showing the viscous response of phase pure C-S-H material without statistical assumptions.

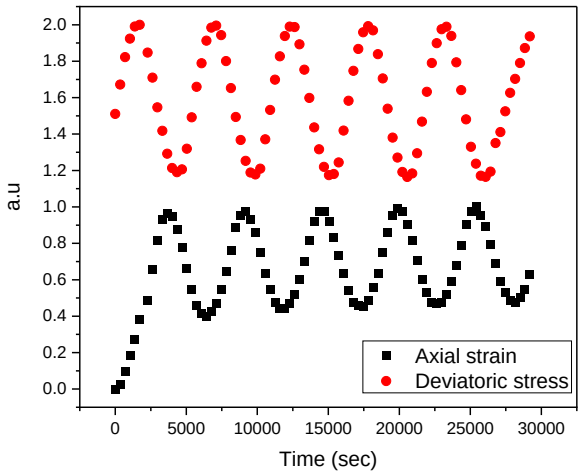

Figure 34 Applied deviatoric stresses and the macroscopic axial strain response of CSH. The viscous behavior of CSH is shown by the delay of the response of the strain

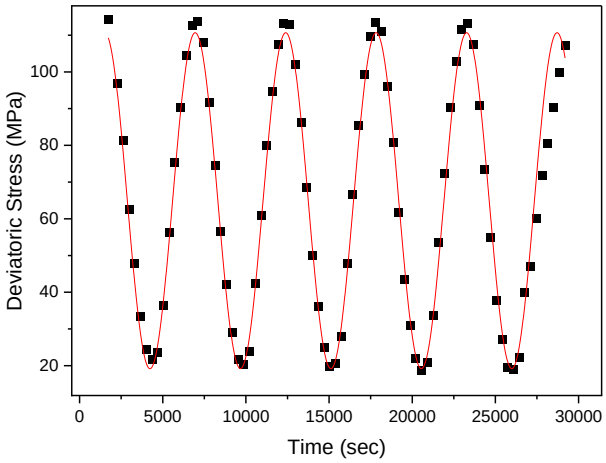

Figure 35 Fittings of the deviatoric stress from the cyclic loadings experiment on C-S-H

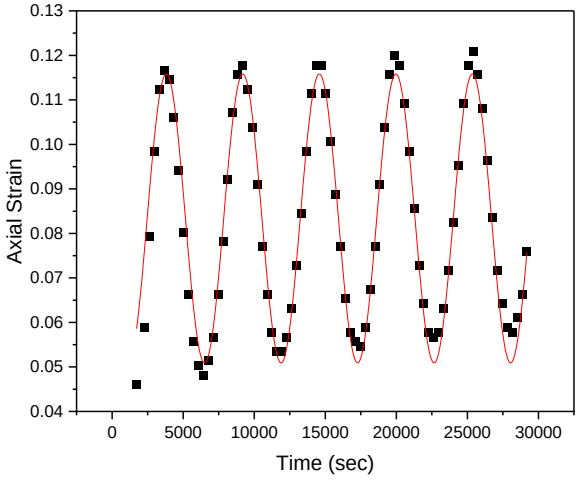

Figure 36 Fittings of the axial strain response from the cyclic loadings experiment on C-S-H

To study orientation behaviors of C-S-H nanoparticles under shear loads, we plot the axial stress-strain curve (Figure 37) of C-S-H contained in the polyacrylic sample holder and monitor the development of textures using pole figures from the analysis of diffraction images recorded at each incremental increase of loadings. The strain rates were controlled between 0.002 to 0.005 % s^{-1} to ensure we capture as many details from diffractions as possible. The (seemingly) abrupt drop of loads measured directly to the hydraulics (oil pressure) when we had to temporarily stop the deformations and retract the differential rams and close the corresponding valves, as the rams had reached the end traveling position; but the loads exerted on the sample was maintained and monitored by additional pressure gauges. After the rams were fully retracted (this process took about 1.5 to 2 hours), we continued to deform the sample again. We resumed the deformations with a slightly lower pressure just before the rams were retracted to ensure minimal disruption to

the deformation process. Moreover, we cautiously compared the diffraction images in the vicinity to the discontinuity point to ensure the texture of the sample was not interrupted. The exponential increase of the axial stresses when the strain reaches about 70% is caused by the breaking of the gold foils on both ends of the sample and not the true mechanical behaviors of the sample.

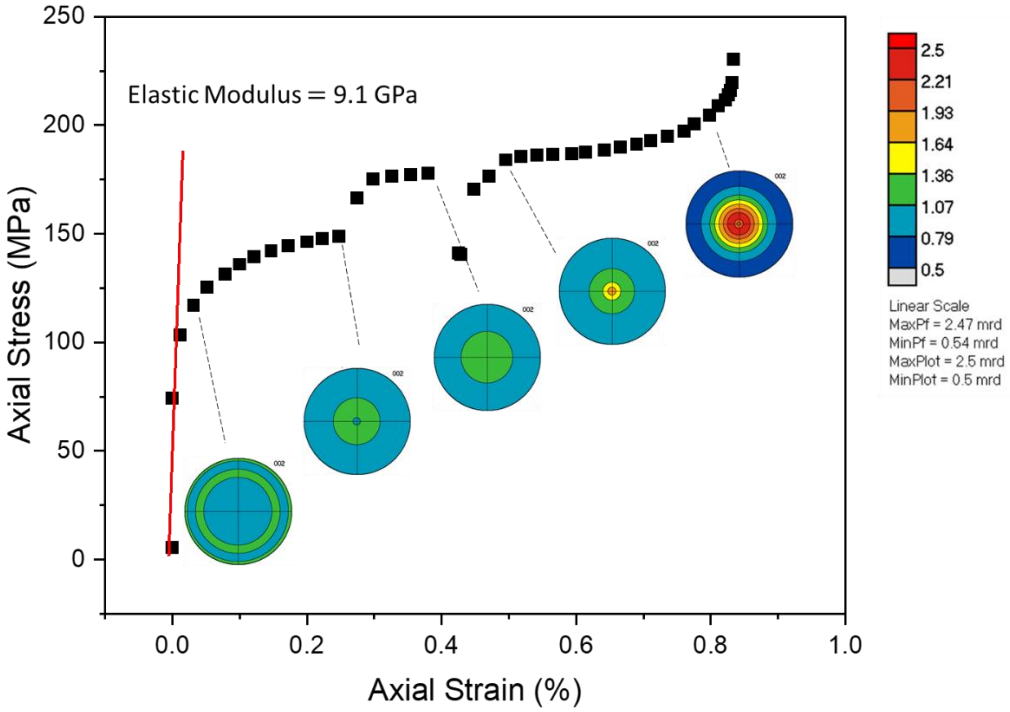

Figure 37 Axial stress and strain curve of C-S-H contained in the polyacrylic sample holder. The sample was confined with hydrostatic stress of 30 MPa followed by a steady increase of uniaxial stress at the strain rate of 0.003 - 0.005 % s-1 until it reached about 225 MPa. The magnitude of the deviatoric stress is approximately 38 MPa lower than the axial stress beyond the first discontinuity point, as an additional ~8 MPa of pressure was needed to apply externally on the differential rams to drive the deformations more smoothly. The pole figures indicate that the C-S-H nanoparticles begin to form texture at axial stress of around 150 MPa (or deviatoric stress of 120 MPa)

4.2 X-ray Diffraction Results

Selected diffraction patterns. The experimental geometry places a two-dimensional detector perpendicular to the direction of the incident x-ray; the Ewald sphere, reciprocal lattice vector, and diffraction center (for a hkl plane) then define a diffraction cone (the observed Debye rings on the detector), see Figure 21. In this geometry, we can almost simultaneously infer the texture

development of C-S-H nanoparticles from the diffraction intensities along the 002 ring as we apply the loads.

At the ambient state (Figure 38a), no texture was observed as indicated by uniform diffraction intensities along the 002 ring, showing also sample preparation did not disrupt the initial random orientation of C-S-H nanoparticles. At hydrostatic state (Figure 38b), C-S-H nanoparticles were still randomly oriented, as expected and in agreement with our previous works.

We first observed an apparent texture of C-S-H nanoparticles after retracting the differential rams and resumed the deformations when deviatoric stress reached approximately 120 MPa, indicated by slightly higher diffraction intensity of the 002 ring along compression direction (shown by blue arrows in Figure 38c). The higher diffraction intensity indicates C-S-H nanoparticles are preferentially oriented such that 002 planes of C-S-H nanocrystals align perpendicular to the compression direction. This intensity steadily increases as we constantly increase the loads. The higher intensity of merged 020 and -220 diffractions (due to the poor crystallinity nature of the sample) perpendicular to the compression direction also indicates the preferred orientation of the C-S-H nanoparticles (Figure 38d).

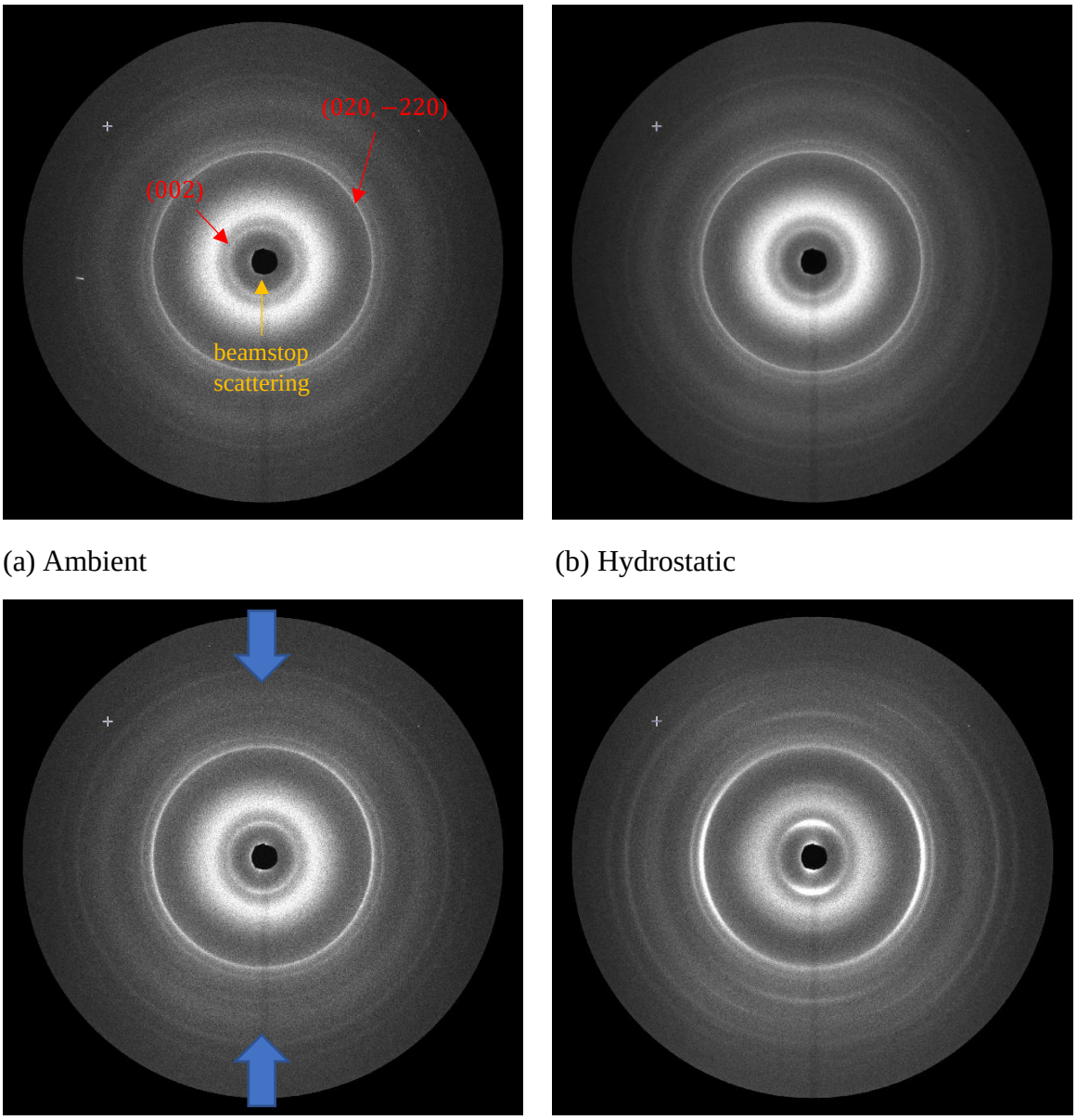

(a) Ambient (b) Hydrostatic

(c) 129 MPa (d) 166 MPa

Figure 38 Monitoring development of texture of C-S-H under loadings with diffraction data. **a** Sample at ambient state, 002 diffraction intensities appear uniform indicating the random orientation of C-S-H nanoparticles. **b** Sample under hydrostatic stress of 30 MPa, 002 diffraction intensities remain uniform. **c** First noticeable diffraction pattern that shows a slight increase of 002 diffraction intensities along compression direction, indicating some preferred orientation of C-S-H nanoparticles. **d** Very strong texture has developed when the applied loads reached 206 MPa, indicated by strong 002 diffraction intensities along compression direction (and strong intensity of merged 022, -220 diffraction perpendicular to the compression direction)

4.3 Texture Analysis

Profiles of Pole Density on (002) pole figure. We plot multiple of random distribution (m.r.d) values as a function of the angle η between 002 normal and the compression axis to quantify the variation of texture strengths as we compressed the sample Figure 39. The m.r.d values are the highest along the compression direction, and the values smoothly decrease as the tilt angles increase. The shape of the profiles of pole density follows the March function.

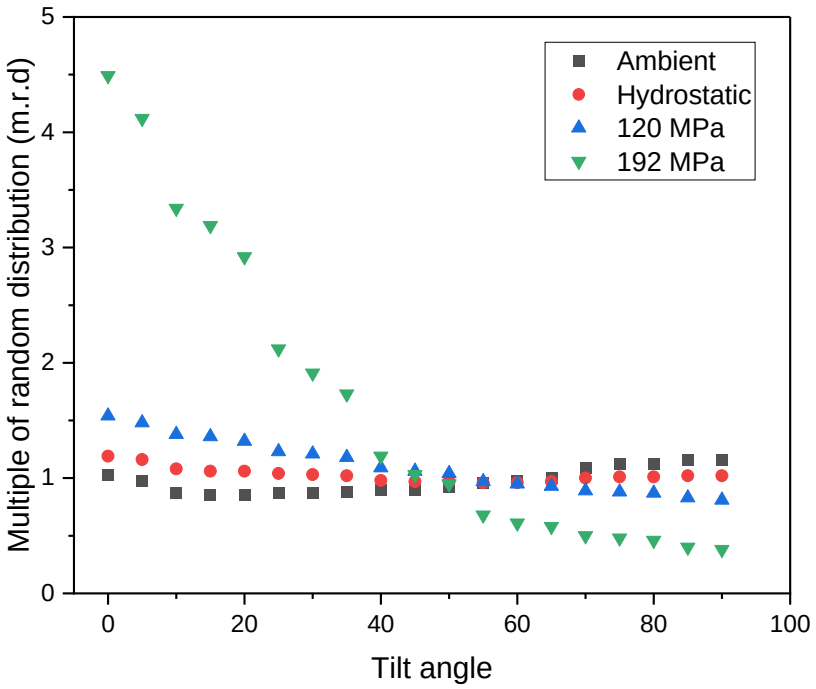

Figure 39 Profiles of pole density on (002) pole figure, as a function of the angle between (002) normal and the compression axis. Multiple of random distribution value of 1 indicates random orientations of C-S-H nanoparticles

Selected Pole Figures

Texture analysis and the results from the pole figures correlate well with qualitative observations of the diffraction images. To quantify the texture, the variation of intensity along the 002 ring was computed by the EWIMV algorithm [89], and assuming the stress field is symmetrical about the compression direction, i.e., $\sigma_{11} = \sigma_{22}$, the cylindrical symmetry (or fiber symmetry) in the Material Analysis Using Diffraction software (MAUD) was applied to produce an orientation distribution (OD) function. The OD function from MAUD was exported to the BEARTEX software [76] and smoothed with a Gaussian filter to minimize artifacts.

Figure 40 a and b show that C-S-H nanoparticles were still randomly oriented at both ambient and hydrostatic pressures, in agreement with previous studies.

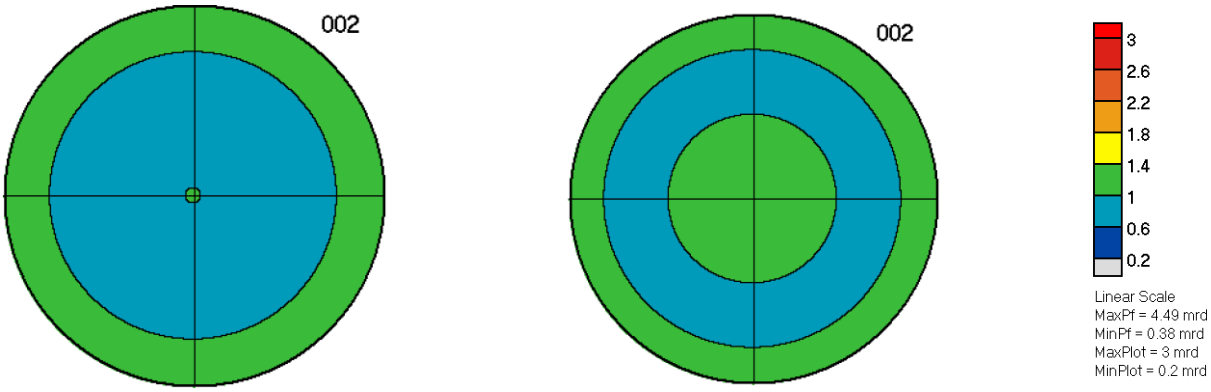

(a) Ambient pressure

(b) Hydrostatic

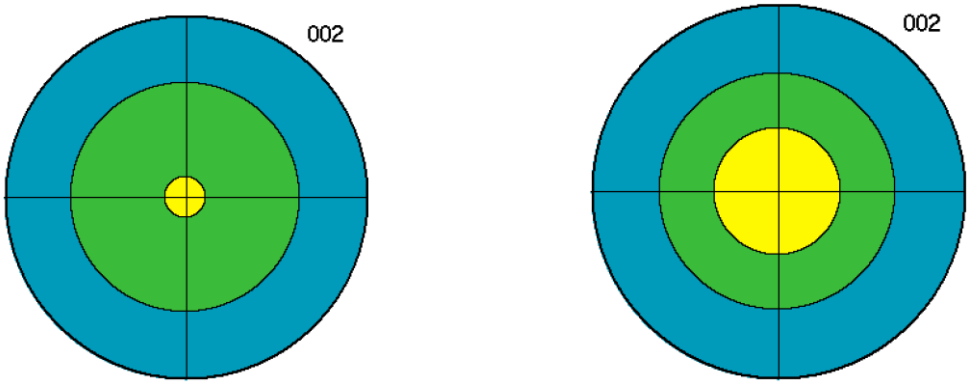

120 MPa

(d) 146 MP

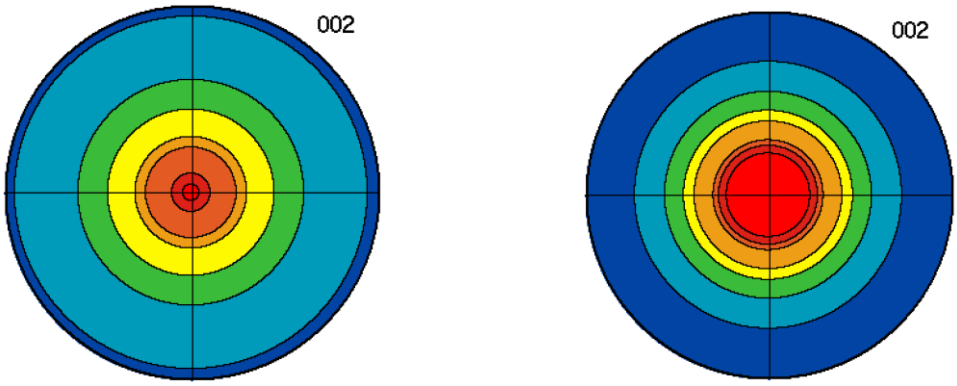

(e) 161 MPa

(f) 192 MPa

Figure 40 Monitoring development of texture of C-S-H under loadings with pole figures. **a** and **b** Maximum m.r.d values are approximately one about the center of the pole figures (the compression direction is perpendicular to the center of the pole figure), indicating the random orientation of C-S-H nanoparticles. **c** First noticeable pole figure that shows maximum m.r.d values increased to approximately 1.4 about the center of the pole figures, indicating a 40% increase of probability to find (002) planes normal to the compression direction compared to when no deviatoric stress is applied. **d-f** texture has steadily developed as we constantly increased loadings; very strong texture has formed at deviatoric stress of approximately 192 MPa

The deformations initially reached about 140 MPa (40% of macroscopic strains) before the differential rams had reached the end traveling position, and we did not observe apparent textures in this period. However, when we resumed the deformations after the differential rams were retracted, we observed the m.r.d values had changed to approximately 1.4 when the deviatoric stresses reach about 120 MPa, indicating weak texture formation but implies a 40% increase of probability to find (002) planes normal to the compression direction compare to when no deviatoric stress is applied. To our knowledge, 120 MPa is the lowest measured deviatoric stress for observing the texture formation of C-S-H nanocrystals directly from the experiment. This result could capture the initiation process of the texture development of C-S-H under shear loadings and may provide some hint related to the energy barrier (or driving force) for rearranging C-S-H nanoparticles in an analog to thermal activation energy theory [90, 91]. Beyond this energy barrier, more C-S-H nanoparticles steadily reorganize as loads increase, evident by the increasing max. m.r.d values shown in the pole figures and appears to asymptotically approach to approximately three at deviatoric stress of roughly 192 MPa. We measured a similar max m.r.d value when applying 1 GPa stress through confined compression on the same C-S-H sample using DAC (unpublished results). The asymptotic maximum m.r.d value may suggest packing density of C-S-H nanocrystals has reached some maximum amount, i.e., further shear loadings beyond 192 MPa begin to deform tightly packed C-S-H nanoparticles but are sustained by the compact packing, and the atomic interactions between silicate chains, calcium ions, and water molecules (or hydroxides).

One reason we did not observe the texture formation during the initial deformations may be due to the "delayed response" of CSH nanoparticles owing to its viscous nature, i.e., the strain rate was too fast before these nanoparticles could reorient to the preferred positions, shown in Figure 34. It requires further experiments, for instance, a series of different strain rates of deformations, to confirm this hypothesis.

We further studied this orientation behavior using the concept of phase transitions in liquid crystals (Su, Dolado, Monteiro, in preparation for a journal publication). A simulation result of the scalar order parameter or S-factor plot of C-S-H under deviatoric stress deformations is shown in Figure 41. S-factor is defined as

$$S = \frac{1}{2}\langle 3\cos(\theta) - 1\rangle$$

where (θ) is the angle between the compression direction and the orientation of one C-S-H nanoparticle, and < > represents the average value of all CSH nanoparticles. The results indicate again that the C-S-H nanoparticles begin to form texture at deviatoric stress of about 120 MPa.

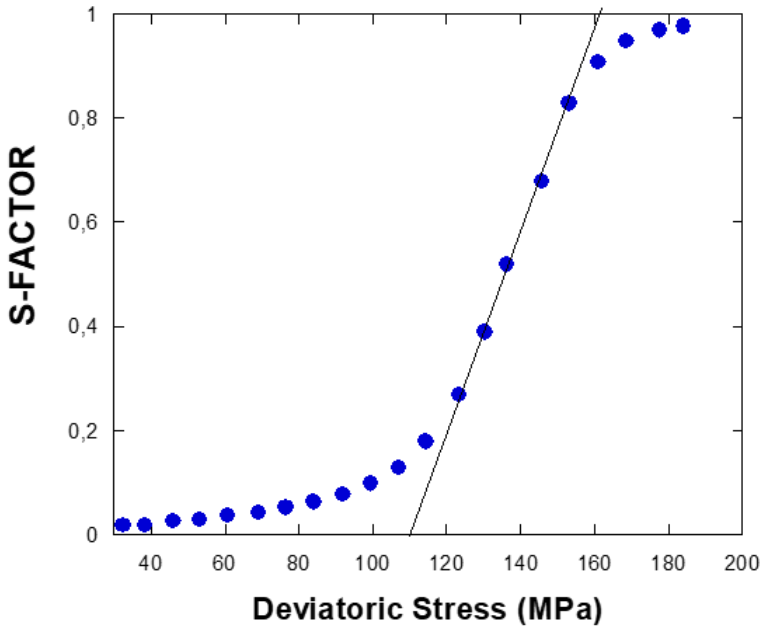

Figure 41 Scalar order parameter plot of C-S-H under deviatoric stress deformations. The simulation results indicate that the C-S-H nanoparticles begin to form texture at deviatoric stress of about 120 MPa (Su, Dolado, Monteiro, in preparation for a journal publication).

We neglected the potential role of water for reorganizing C-S-H nanoparticles under loads in this study, where water has been debated to play a crucial role in concrete creep. For example, based on viscous shear theory [92], adsorbed water could be a lubricant for C-S-H nanoparticles to slip under shear. Therefore, it is reasonable to hypothesize that the texture strength may be affected under different relative humidity (RH) conditions. Our approach of applying HPXRD experiments to study orientation behaviors of C-S-H under loadings could be modified by controlling RH around the sample environment and potentially be a valid method to test the role of water in concrete creep.

Gardner et al. applied high-pressure Raman spectroscopy to probe Si-O interaction in C-S-H samples with different interlayer water content under hydrostatic deformations [93]. The measured and calculated bond anharmonicities prove to be valuable in determining the change of molecular interactions in C-S-H when under loads. However, the experiment adopted DAC and suffers some limitations described in 2.5.1.

We also noticed that the degree of preferred orientation of C-S-H nanoparticles is not directly proportional to the applied loads when comparing the measured m.r.d values with different pressure medium materials; however, since experimental conditions were not identical in these experiments, further investigations are needed to verify the observations.

Finally, it requires some experience in selecting the pressure medium (sample holder material) for HPXRD experiments at beamline 13-BM-D, and one of the essential criteria to consider is the material's yield strength. However, due to the viscoelastic behavior of polymeric pressure medium materials, the yield strengths could vary and be sensitive to strain rates and the operation temperature, which adds another layer of complexity to the experiment. Separating viscoelastic responses attributed by C-S-H and polymer pressure medium can be challenging. This study assumes the loads exerted on the pressure medium were uniformly transmitted to the sample; potential anisotropic behavior and stress relaxation from the polymer pressure medium were neglected.

By contrast with our previous works on studying the preferred orientation of a more crystalline C-(A-)S-H sample – which was intentionally synthesized at higher temperature [69], the present work has used a poorly crystalline C-S-H sample synthesized at room temperature and is a closer representation to the C-S-H found in the real hydrated cement paste. The result opens a new perspective in understanding C-S-H; for example, if rearrangement of C-S-H nanoparticles is the root cause of concrete creep, then the degree of preferred orientation measured by HPXRD experiments may be used to validate some of the existing theories of C-S-H creep mechanisms. A deeper understanding of structure-property relationships of C-S-H may then offer a new approach for designing more durable concrete materials from the bottom-up.

Chapter Five: Shear Deformations of Modified-CSH Nanocomposites

5.1 Cyclic Loadings Experiments on Modified-CSH Nanocomposites

Two modified C-S-H nanoparticles with APTES using different synthetic methods were investigated with the HP-XRD technique at the beamline 13-BM-D at APS; the experimental setup and conditions are similar to the experiment described in Chapter Four. Figure 42 and Figure 43 show the stress and strain results of the cyclic loadings experiment on CSH-APTES A and CSH-APTES B samples, respectively, and illustrate the material's apparent viscoelastic behavior.

The storage modulus of CSH-APTES A and CSH-APTES B samples are computed from the fittings shown in Figure 44 to Figure 47, and the fittings use a sinusoidal wave function to simulate the stress and the strain response. The modulus values are 463.27 MPa and 578.68 MPa, for CSH-APTES A and CSH-APTES B, respectively; the pores in the sample volume space most likely contributed to the low stiffness values. However, the results successfully demonstrate that HP-XRD is a powerful technique to investigate cementitious materials' highly complex viscoelastic behavior.

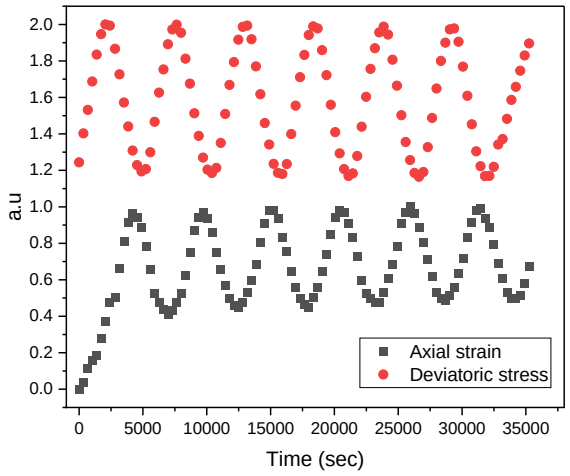

Figure 42 Applied deviatoric stresses and the macroscopic axial strain response of CSH-APTES A. The viscous behavior of the sample is shown by the delay of the response of the strain

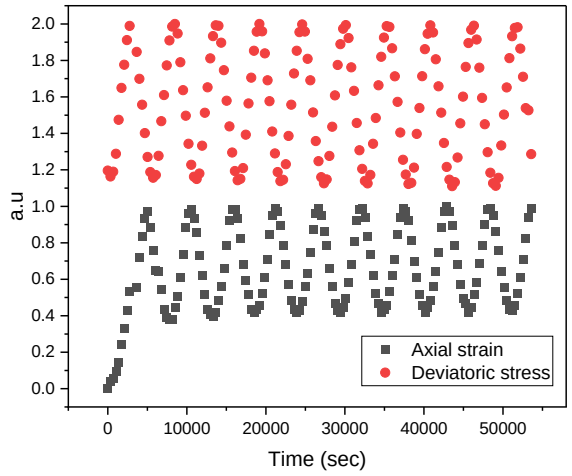

Figure 43 Applied deviatoric stresses and the macroscopic axial strain response of CSH-APTES B. The viscous behavior of the sample is shown by the delay of the response of the strain

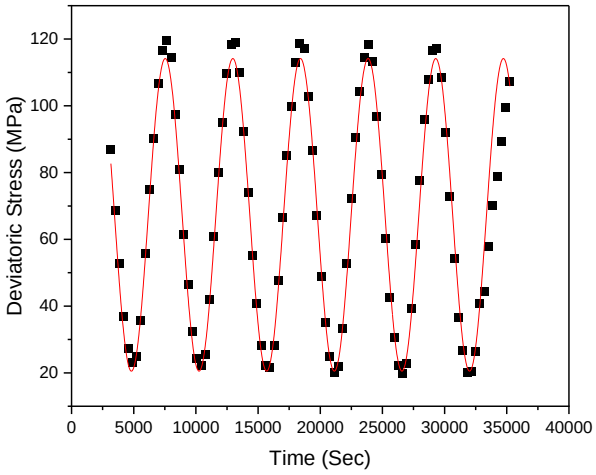

Figure 44 Fittings of the deviatoric stress from the cyclic loadings experiment on CSH-APTES A

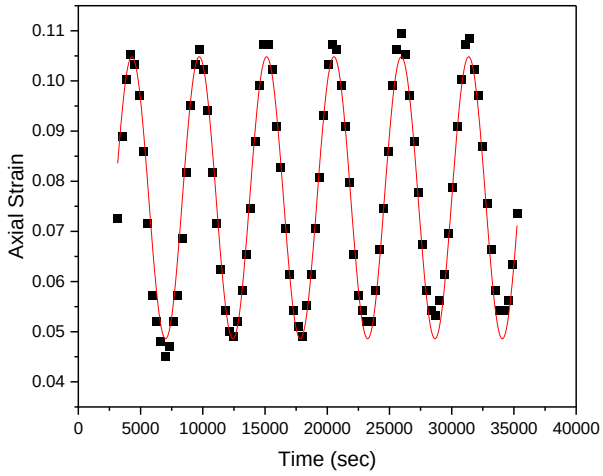

Figure 45 Fittings of the axial strain response from the cyclic loadings experiment on CSH-APTES A

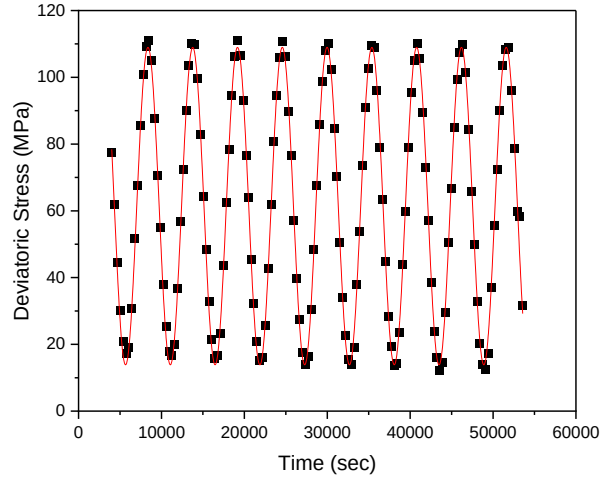

Figure 46 Fittings of the deviatoric stress from the cyclic loadings experiment on CSH-APTES B

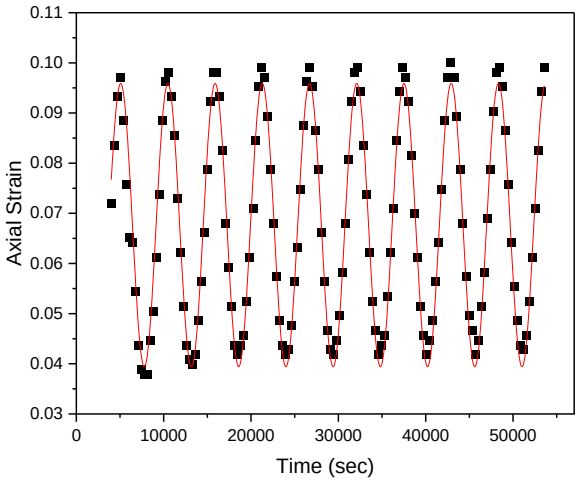

Figure 47 Fittings of the axial strain response from the cyclic loadings experiment on CSH-APTES B

The stress versus strain behavior of CSH-APTES A and CSH-APTES B samples are shown in Figure 48 and Figure 49, respectively. The deformation conditions, such as strain rates, were similar to the deformation experiment of CSH described in Chapter Four. The amount of deformation is limited by the potential collapse of the anvils when they are in close proximity, and therefore, stopped at around 60% of the strains for both experiments.

Note the (seemingly) abrupt drop of the deviatoric stresses in both figures, which correspond to the retraction of differential rams when the rams reached the end traveling position. In the deformation experiment of the CSH-APTES B sample, the experiment was interrupted by the temporary blackout of the synchrotron sources, adding another apparent discontinuity point at around 34% of the strain. We cautiously compared the diffraction data in the vicinity to all the discontinuity points to ensure the texture of the sample was not being interrupted.

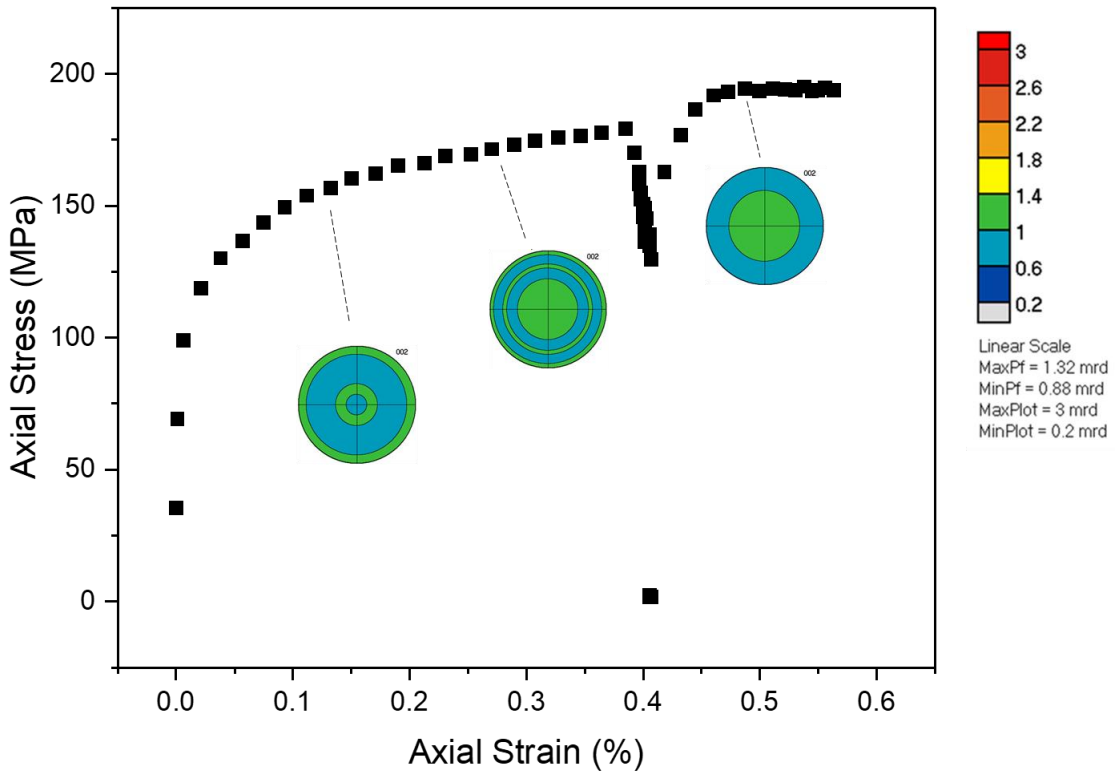

Figure 48 Axial stress and strain curve of CSH-APTES A contained in the polyacrylic sample holder. The sample was confined with hydrostatic stress of 30 MPa followed by a steady increase of uniaxial stress at the strain rate of 0.003 - 0.005 % s^{-1}. The magnitude of the deviatoric stress is approximately 28.9 MPa lower than the axial stress. The pole figures indicate that the C-S-H nanoparticles begin to form texture at axial stress of around 167 MPa (or deviatoric stress of 138 MPa)

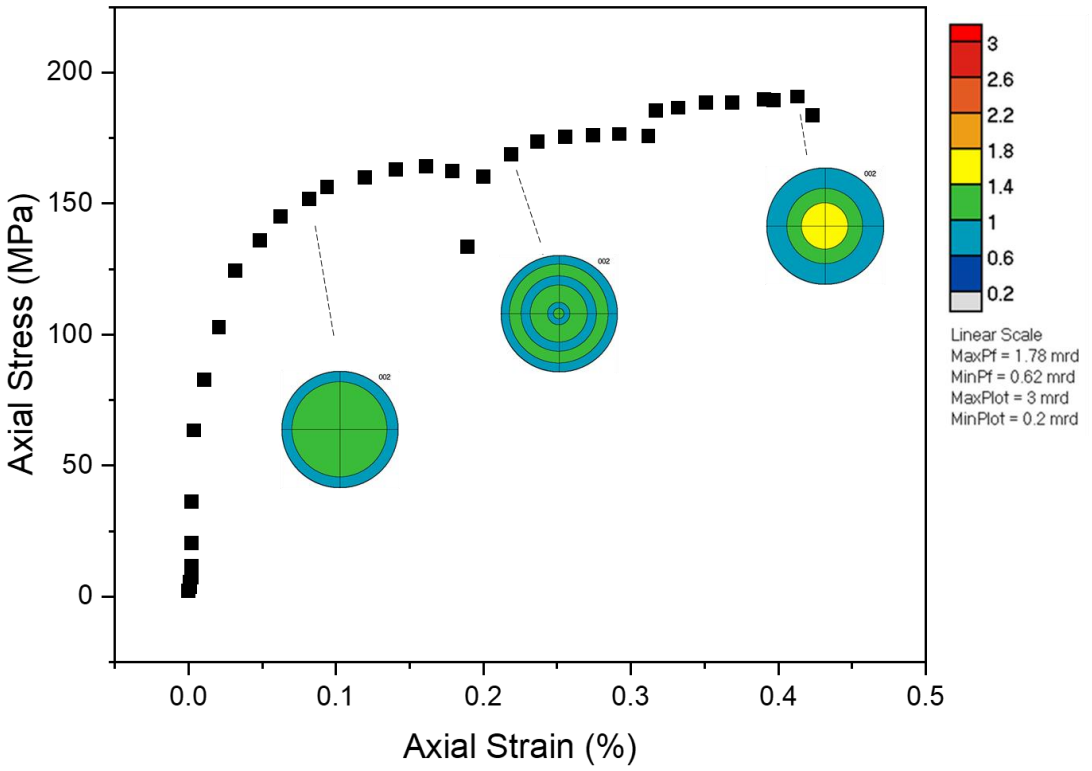

Figure 49 Axial stress and strain curve of CSH-APTES B contained in the polyacrylic sample holder. The sample was confined with hydrostatic stress of 30 MPa followed by a steady increase of uniaxial stress at the strain rate of 0.003 - 0.005 % s^{-1}. The magnitude of the deviatoric stress is approximately 29 MPa lower than the axial stress. The pole figures indicate that the C-S-H nanoparticles begin to form texture at axial stress of around 176 MPa (or deviatoric stress of 147 MPa)

5.2 X-ray Diffraction Results

Selected diffraction patterns. The experimental geometry and conditions for both CSH-APTES A and CSH-APTES B samples, such as the energy of x-rays, strain rates and exposure time etc., were similar to the experiment on CSH described in Chapter Four. The diffractions contain boron nitride due to the sample preparations.

At the ambient state, no apparent texture was observed as indicated by uniform diffraction intensities along the 002 ring shown in Figure 50 and Figure 51, confirming that sample preparations did not disrupt the initial random orientation of C-S-H nanoparticles. Furthermore, both samples were still randomly oriented at hydrostatic state, agreeing with the previous works.

CSH-APTES A first shows an apparent texture at deviatoric stress of approximately 138 MPa, indicated by slightly higher diffraction intensity of the 002 ring along compression direction (Figure 50). While CSH-APTES B first shows an apparent texture at deviatoric stress of approximately 147 MPa (Figure 51). However, the corresponding max. m.r.d values are only 1.24 and 1.25 for CSH-APTES A and CSH-APTES B, respectively, indicating relatively weak textures had developed for both modified-CSH nanoparticles and suggesting higher deviatoric stresses are needed to rearrange CSH-APTES nanocomposites.

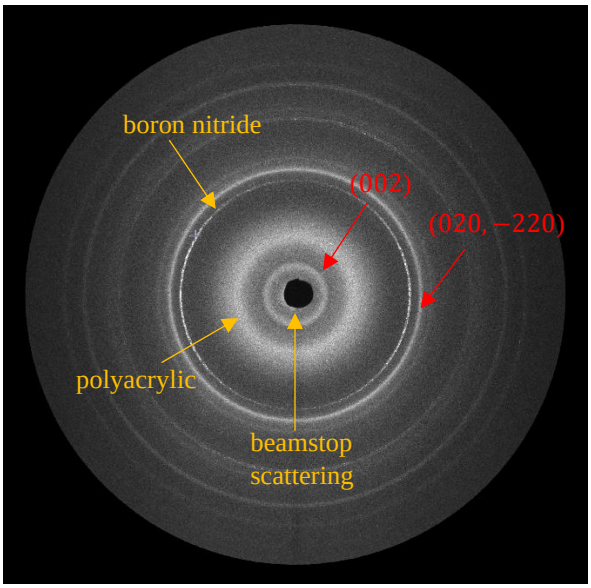

Ambient

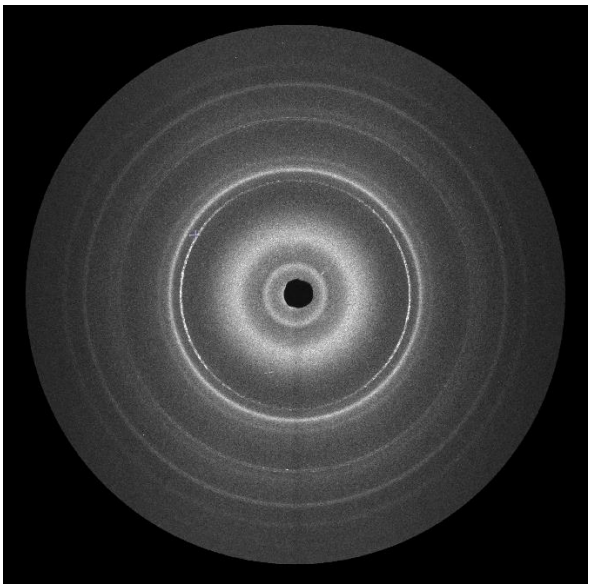

Hydrostatic

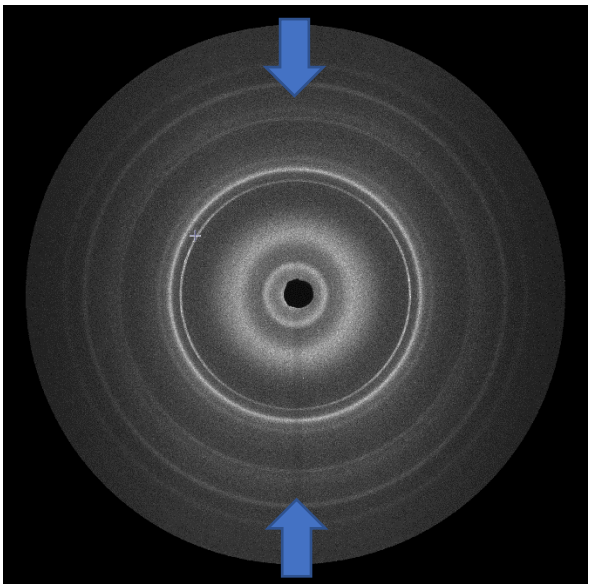

138 MPa

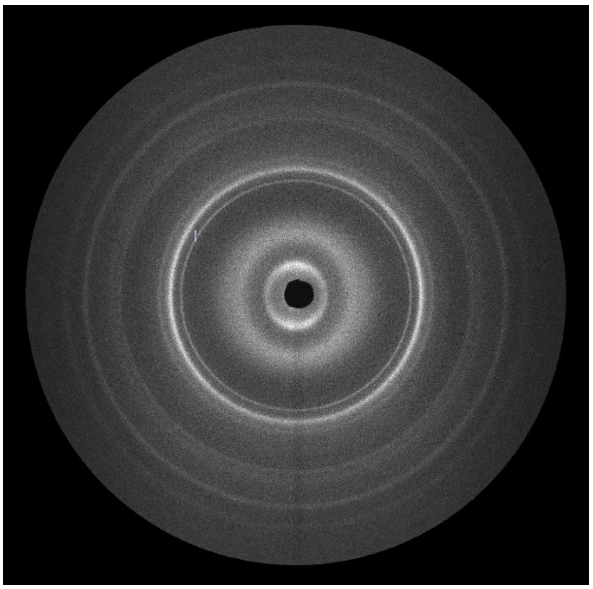

165 MPa

Figure 50 Monitoring development of texture of CSH-APTES A under loadings with diffraction data. **a** Sample at ambient state, 002 diffraction intensities appear uniform indicating the random orientation of the nanoparticles. The diffractions contain boron nitride due to the sample preparation. **b** Sample under hydrostatic stress of 30 MPa, 002 diffraction intensities remain uniform. **c** The nanoparticles remain randomly oriented at the deviatoric stress of about 138 MPa. **d** Texture developed when the applied loads reached 165 MPa, indicated by strong 002 diffraction intensities along compression direction

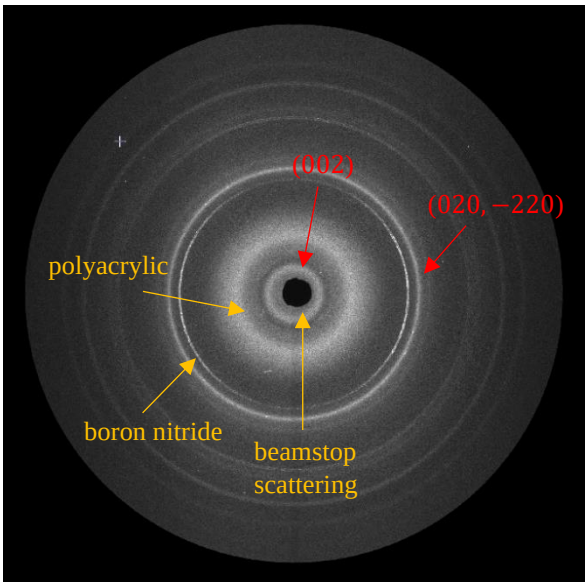

Ambient

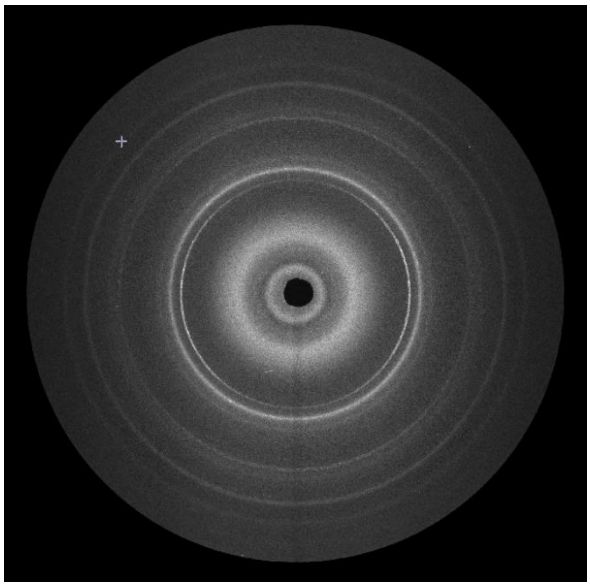

Hydrostatic

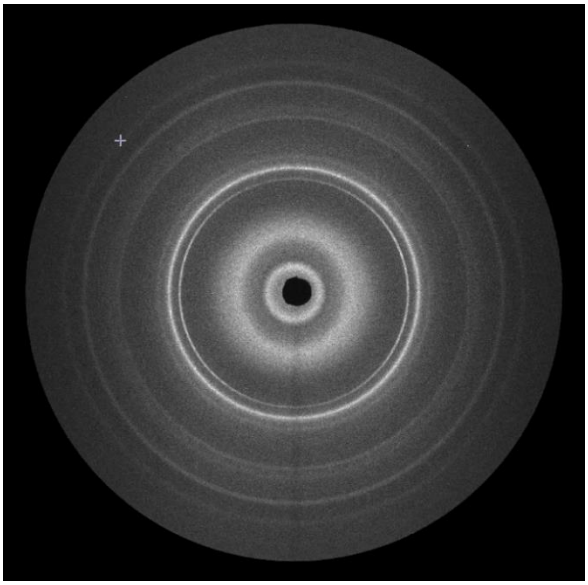

147 MPa

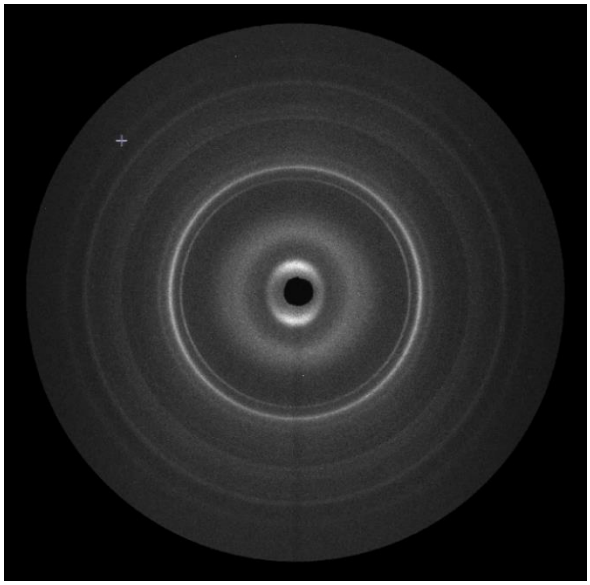

160 MPa

Figure 51 Monitoring development of texture of CSH-APTES B under loadings with diffraction data. **a** Sample at ambient state, 002 diffraction intensities appear uniform indicating the random orientation of the nanoparticles. The diffractions contain boron nitride during sample preparation. **b** Sample under hydrostatic stress of 30 MPa, 002 diffraction intensities remain uniform. **c** The nanoparticles remain randomly oriented at the deviatoric stress of about 147 MPa. **d** Texture has developed when the applied loads reached 160 MPa, indicated by strong 002 diffraction intensities along compression direction

5.3 Texture Analysis

Selected Pole Figures. Figure 52, 54, and 56 show profiles of pole density on (002) pole figures, as a function of the angle between (002) normal and the compression axis of C-S-H, CSH-APTES A, and CSH-APTES B samples, respectively at the following selected pressures, 130, 140, 150, and 160 MPa. The corresponding pole figures are shown in Figure 53, 55, and 57.

The unmodified C-S-H sample is prone to develop textures as compared with both modified CSH-APTES samples. The results show that the max. m.r.d value of C-S-H is 20.6% higher than both modified CSH-APTES samples at deviatoric stress of around 130 MPa, and when the deviatoric stress reaches 150 MPa, the max. m.r.d value of C-S-H is 39.9% higher than CSH-APTES A and 38.3% higher than CSH-APTES B (Table 3 and Figure 58). These results imply the following consequences: (1) a noticeable increase of the deviatoric stresses is required to drive the "initiation" process of forming textures for the CSH nanoparticles. (2) after this initiation process (when passing the energy barrier to reorganize CSH nanoparticles), the higher deviatoric stresses are required to rearrange modified CSH nanoparticles and increase their max m.r.d values, i.e., both CSH-APTES samples show more resistance to develop preferred orientations under deviatoric stresses as compared to unmodified CSH sample.

Table 3 Max. m.r.d values of different CSH samples at selected deviatoric stresses

	C-S-H max. m.r.d	**CSH-APTES A max. m.r.d**	**CSH-APTES B max. m.r.d**
130 MPa	1.36	1.08	1.08
140 MPa	1.35	1.03	1.11
150 MPa	1.93	1.16	1.19
160 MPa	2.38	1.32	1.78

Chapter Three presented the DAC results of both modified CSH-APTES samples (see Table 2) and discussed some aspects of the nanocomposites' stability in kinetics and thermodynamics. Relative to the unmodified C-S-H sample, the bulk moduli increased by 66.4% and 60.4% for CSH-APTES A and CSH-APTES B, respectively, while the basal spacings also increased by 36.8% and 53.7% for both modified samples, which implies the intercalations of the APTES molecules.

It is evident from these results that the structural differences and the different chemical stabilities and modifications of the nanostructures of C-S-H can effectively change its orientation behaviors under deviatoric stresses. The max. m.r.d value of CSH-APTES A is only 1.32 at deviatoric stress of around 160 MPa, lower than CSH-APTES B sample's max. m.r.d value of 1.78 at similar stresses. The results further indicate that a more tightly-packed CSH-APTES A sample not only appears to be more chemically stable but also shows the largest resistance to the rearrangement of nanoparticles under shear loadings. Consequently, if rearrangement of C-S-H nanoparticles is the

root cause of concrete creep, the intercalation of small organic molecules into the layered structure of C-S-H proves to be a promising approach to designing a more creep-resistant concrete. It is reasonable to hypothesize that the molecular interactions of the intercalated molecules with the CSH silicate layers could be a significant factor influencing the resultant material's mechanical properties and behaviors.

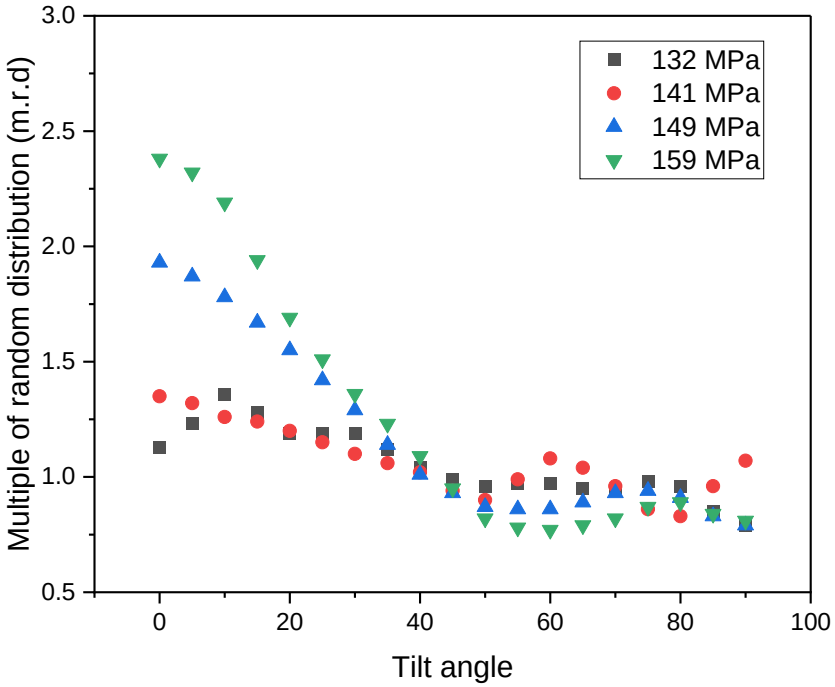

Figure 52 Profiles of pole density on (002) pole figure, as a function of the angle between (002) normal and the compression axis for C-S-H. Multiple of random distribution value of 1 indicates random orientations of C-S-H nanoparticles

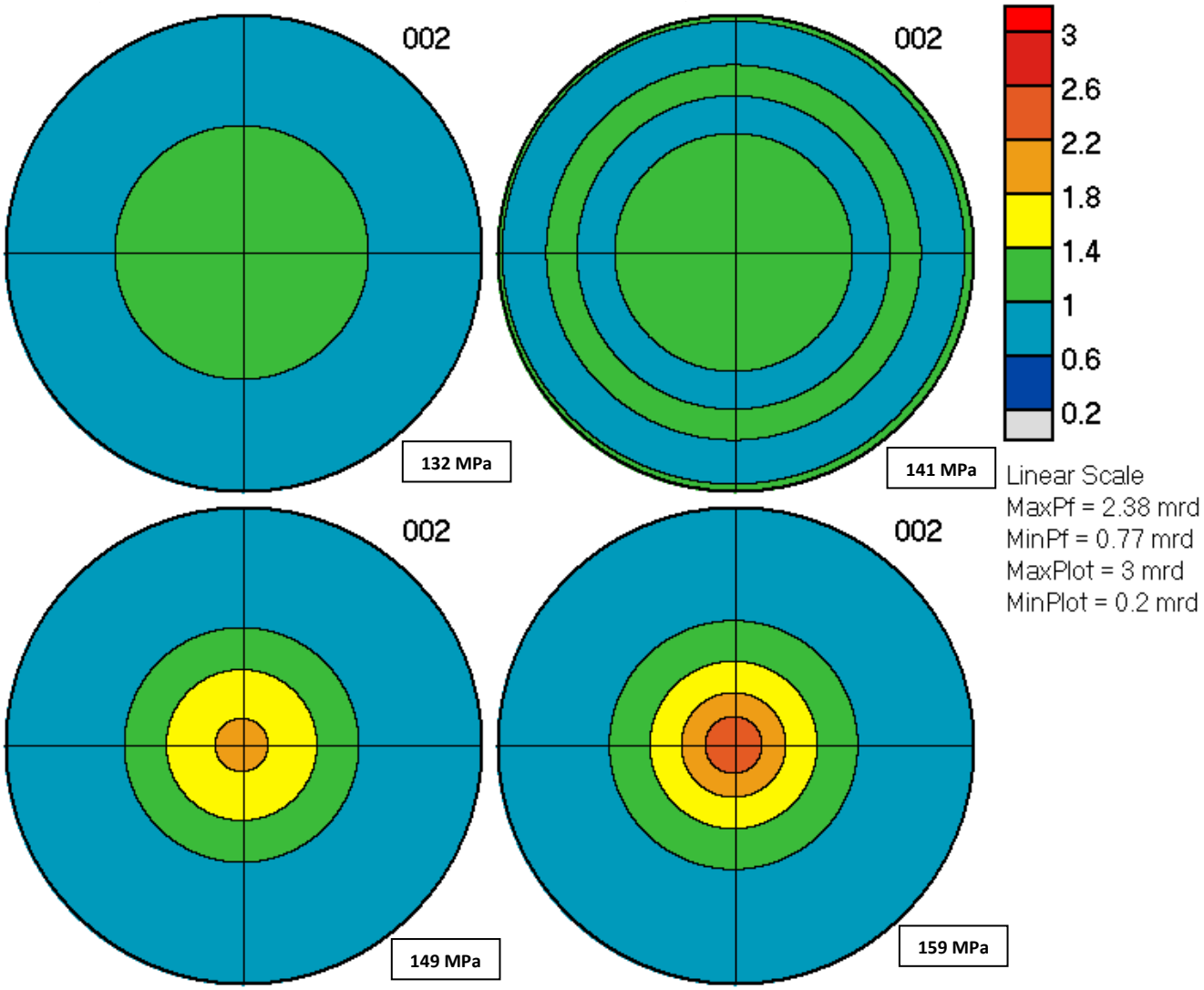

Figure 53 Monitoring development of texture of C-S-H under loadings with pole figures

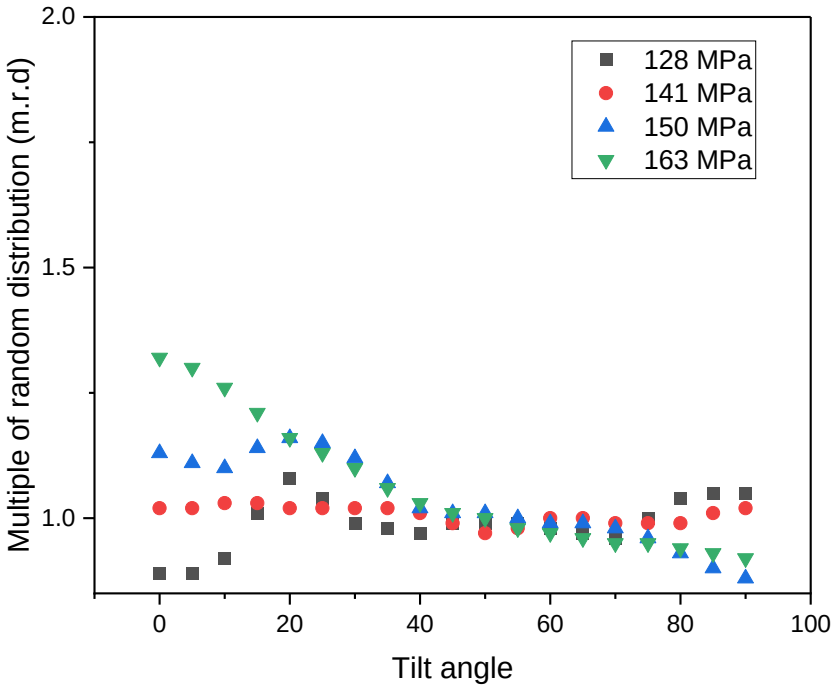

Figure 54 Profiles of pole density on (002) pole figure, as a function of the angle between (002) normal and the compression axis for CSH-APTES A. Multiple of random distribution value of 1 indicates random orientations of CSH-APTES A nanoparticles

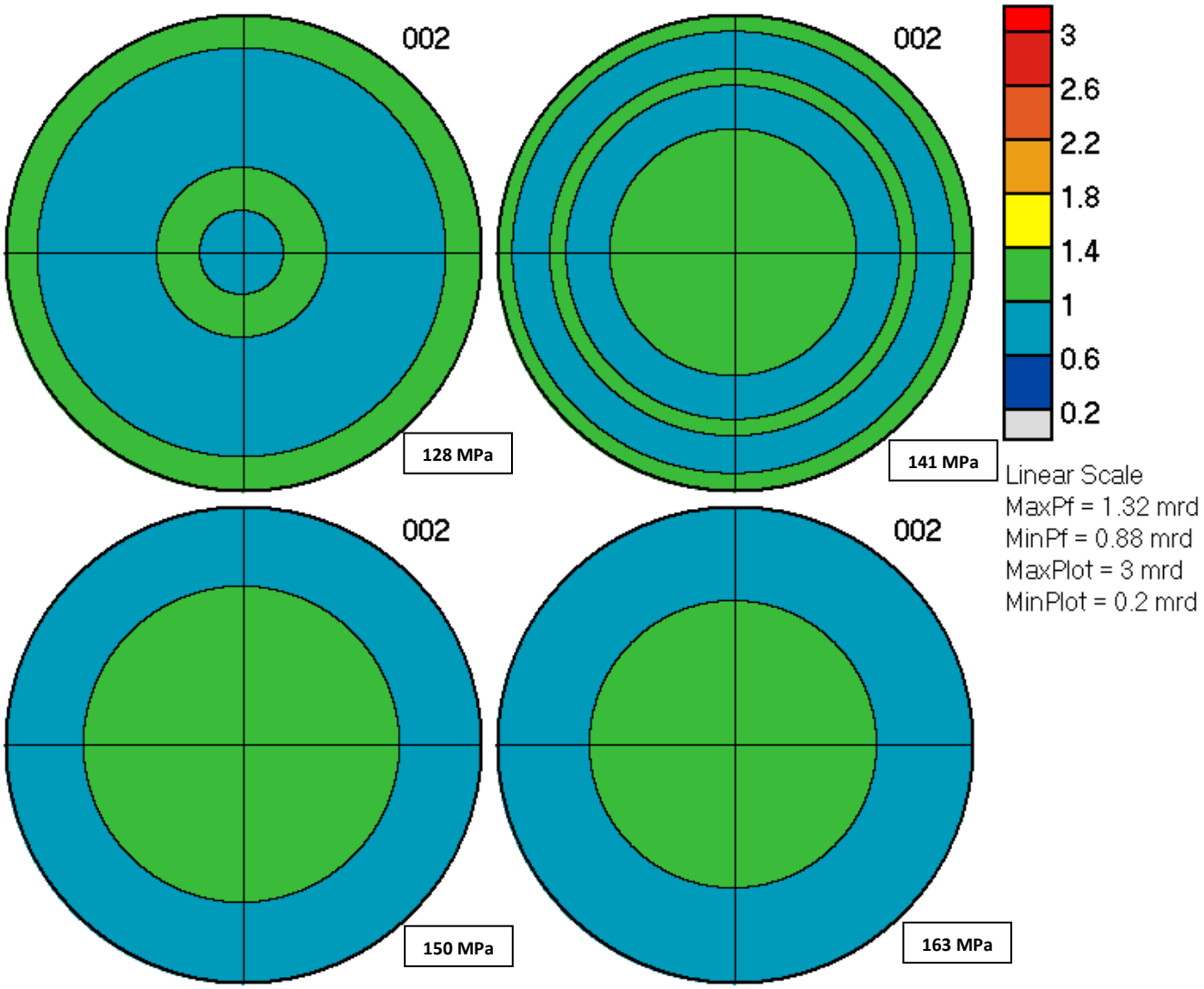

Figure 55 Monitoring development of texture of CSH-APTES A under loadings with pole figures

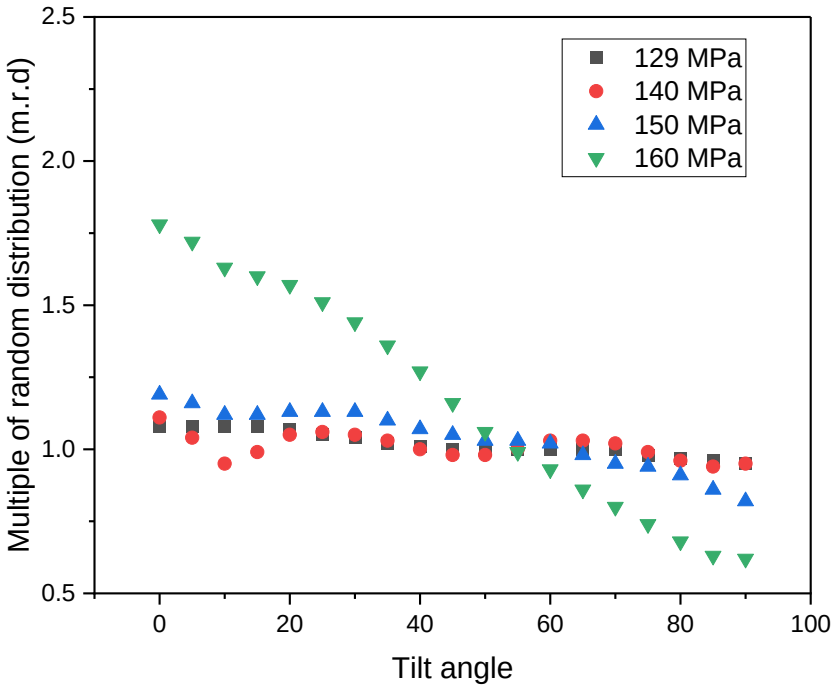

Figure 56 Profiles of pole density on (002) pole figure, as a function of the angle between (002) normal and the compression axis for CSH-APTES B. Multiple of random distribution value of 1 indicates random orientations of CSH-APTES B nanoparticles

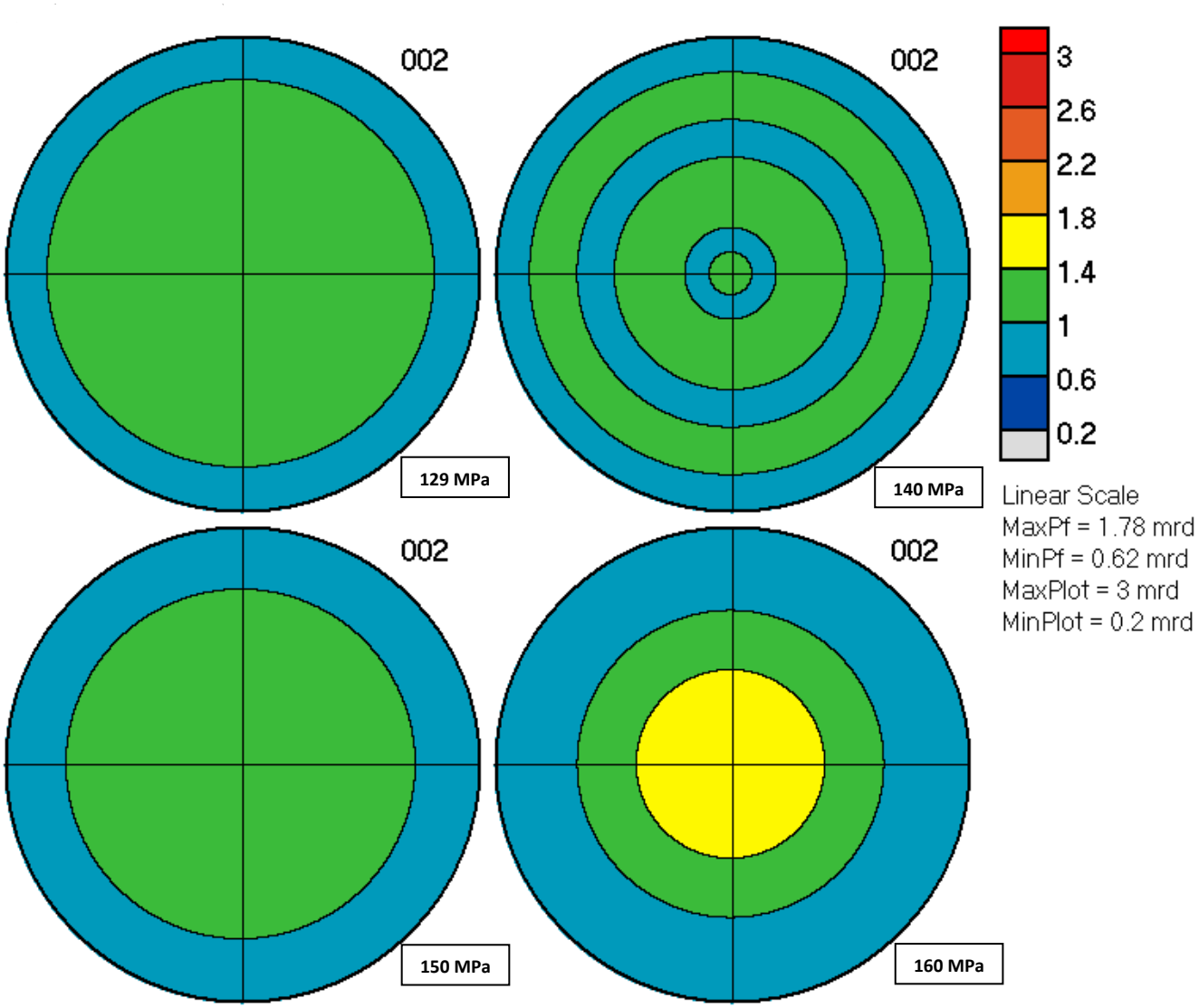

Figure 57 Monitoring development of texture of CSH-APTES B under loadings with pole figures

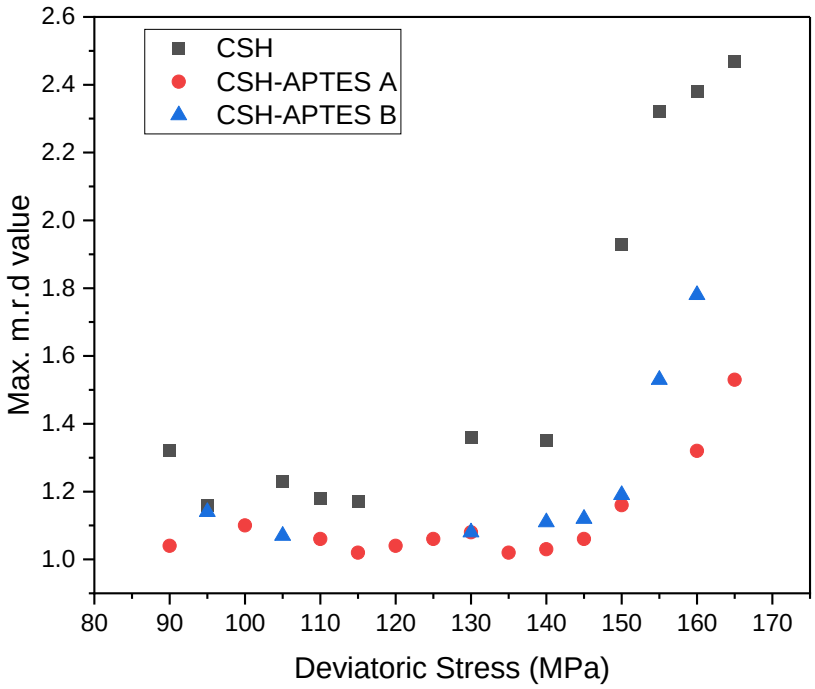

Figure 58 Comparisons of max m.r.d values of different C-S-H samples as a function of deviatoric stress

Chapter Six: Summary and Future Research

The mechanical properties of three different modified-CSH nanocomposites were investigated using DAC in Chapter Three. The experimental results show that the intercalations of APTES molecules into C-S-H basal spacings produce more chemical stable structures and higher bulk modulus nanocomposites than phase pure C-S-H and CSH-PCE nanocomposites. Contrary to previous studies, this work shows apparent intercalations of PCEs into C-S-H basal spacings, given the correct pH conditions and sufficient reaction time. Different thermodynamic forces appear to change the resultant structures differently over time. For the CSH-PCE, the basal spacings became too poorly organized to be measured by x-ray diffraction over twelve months, possibly due to the disruptions of the rearrangements of polymer chains. On the other hand, the basal peaks of the CSH-APTES samples became sharp and intense, indicating the material has increased crystallinity along the c-axis over time. Much understanding in both kinetics and thermodynamics that govern the formations of the modified-CSH nanocomposites is needed.

In Chapter Four, cyclic loading experiments and shear loading deformations on the phase pure C-S-H materials were conducted using D-DIA multi-anvil apparatus. These experiments successfully overcome some major limitations of the previous studies on C-S-H using DAC. The measured deviatoric stress and macroscopic axial strain response from the cyclic loadings reveal the viscous behavior of C-S-H, and texture analysis from shear loading shows for the first time that C-S-H nanoparticles could start forming texture at the deviatoric stress of approximately 120 MPa. The result opens a new perspective in understanding C-S-H and demonstrates that HP-XRD is a valuable technique to investigate some of the existing theories of C-S-H creep mechanisms.

Chapter Five conducts similar cyclic loading experiments and shear loading deformations on the CSH-APTES nanocomposites. The results demonstrate that CSH-APTES samples show more resistance to developing preferred orientations under deviatoric stresses than unmodified CSH samples. Higher deviatoric stresses are also required to drive the "initiation" process of forming textures for the modified-CSH nanoparticles. These findings imply that the intercalation of small organic molecules into the layered structure of C-S-H could be a promising approach to designing a more creep-resistant concrete.

In conclusion, this dissertation applies HP-XRD techniques and the Rietveld refinement method to study the structure-property relationships of C-S-H and modified-CSH nanocomposites. The state-of-the-art synchrotron facilities allow this research to address some long-existing queries in concrete materials. Nevertheless, it remains a significant challenge to understand the creep mechanisms of C-S-H and concrete fully. Some recommended future works to utilize HP-XRD techniques could involve investigating more sophisticated C-S-H nanocomposites and deforming C-S-H with more complex cyclic loading protocols. Moreover, other synchrotron characterization techniques, such as x-ray spectroscopy and scanning transmission x-ray microscopy, could be

coupled with atomistic simulations and better understand the molecular interactions within C-S-H nanoparticles.

References

[1] P. J. Monteiro, S. A. Miller and A. Ho, "Towards sustainable concrete," *Nature Materials,* vol. 16, no. 7, pp. 698-699, 2017.

[2] M. Vandamme and F.-J. Ulm, "Nanogranular origin of concrete creep," *Proceedings of the National Academy of Sciences,* vol. 106, no. 26, pp. 10552-10557, 2009.

[3] R.-M. Pellenq, N. Lequeux and H. Van Damme, "Engineering the bonding scheme in C-S-H: The iono-covalent framework," *Cement and Concrete Research,* vol. 38, no. 2, pp. 159-174, 2008.

[4] K. P. Mehta and P. J. Monteiro, Concrete: microstructure, properties, and materials, McGraw-Hill Education, 2014.

[5] H. F. Taylor, "Proposed structure for calcium silicate hydrate gel," *Journal of the American Ceramic Society,* vol. 69, no. 6, pp. 464-467, 1986.

[6] S. Merlino, E. Bonaccorsi and T. Armbruster, "The real structure of tobermorite 11Å: normal and anomalous forms, OD character and polytypic modifications," *European Journal of Mineralogy,* vol. 13, no. 3, pp. 577-590, 2001.

[7] E. Bonaccorsi, S. Merlino and A. R. Kampf, "The crystal structure of tobermorite 14 Å (plombierite), a C–S–H phase," *Journal of the American Ceramic Society ,* vol. 88, no. 3, pp. 505-512, 2005.

[8] G. Geng, R. J. Myers, J. Li, R. Maboudian, C. Carraro, D. A. Shapiro and P. J. Monteiro, "Aluminum-induced dreierketten chain cross-links increase the mechanical properties of nanocrystalline calcium aluminosilicate hydrate," *Scientific Reports,* vol. 7, no. 1, pp. 1-10, 2017.

[9] A. J. Allen, J. J. Thomas and H. M. Jennings, "Composition and density of nanoscale calcium–silicate–hydrate in cement," *Nature Materials,* vol. 6, no. 4, pp. 311-316, 2007.

[10] L. B. Skinner, S. R. Chae, C. J. Benmore, H. Wenk and P. J. Monteiro,, "Nanostructure of calcium silicate hydrates in cements," *Physical Review Letters,* vol. 104, no. 19, p. 195502, 2010.

[11] K. Garbev, G. Beuchle, M. Bornefeld, L. Black and P. Stemmermann, "Cell dimensions and composition of nanocrystalline calcium silicate hydrate solid solutions. Part 1: synchrotron-based X-ray diffraction," *Journal of the American Ceramic Society,* vol. 91, no. 9, pp. 3005-3014, 2008.

[12] T. E. Rodriguez, I. G. Richardson, L. Black, E. Boehm-Courjault, A. Nonat and J. Skibsted, "Composition, silicate anion structure and morphology of calcium silicate hydrates (CSH) synthesised by silica-lime reaction and by controlled hydration of tricalcium silicate (C_3S)," *Advances in Applied Ceramics,* vol. 114, no. 7, pp. 362-371, 2015.

[13] T. C. Powers and T. L. Brownyard, "Studies of the physical properties of hardened Portland cement paste," *Journal Proceedings,* vol. 43, no. 9, pp. 101-132, 1946.

[14] T. C. Powers, "Structure and physical properties of hardened Portland cement paste," *Journal of the American Ceramic Society,* vol. 41, no. 1, pp. 1-6, 1958.

[15] T. C. Powers, "The thermodynamics of volume change and creep," *Matériaux et Construction,* vol. 1, no. 6, pp. 487-507, 1968.

[16] Z. P. Bažant, A. B. Hauggaard, S. Baweja and F. J. Ulm, "Microprestress-solidification theory for concrete creep. I: Aging and drying effects," *Journal of Engineering Mechanics,* vol. 123, no. 11, pp. 1188-1194, 1997.

[17] Z. P. Bažant, "Prediction of concrete creep and shrinkage: past, present and future," *Nuclear Engineering and Design,* vol. 203, no. 1, pp. 27-38, 2001.

[18] F. H. Wittmann, "Interaction of hardened cement paste and water," *Journal of the American Ceramic Society,* vol. 56, no. 8, pp. 409-415, 1973.

[19] F. H. Wittmann and P. E. Roelfstra, "Total deformation of loaded drying concrete," *Cement and Concrete Research,* vol. 10, no. 5, pp. 601-610, 1980.

[20] W. Ruetz, "A hypothesis for the creep of hardened cement paste and the influence of simultaneous shrinkage," *Proceedings of the Structure of Concrete and its Behavior under Load,* pp. 365-387, 1968.

[21] H. M. Jennings, "Refinements to colloid model of CSH in cement: CM-II," *Cement and Concrete Research,* vol. 38, no. 3, pp. 275-289, 2008.

[22] H. M. Jennings, "Colloid model of C-S-H and implications to the problem of creep and shrinkage," *Materials and Structures,* vol. 37, no. 1, pp. 59-70, 2004.

[23] H. Ye, "Creep mechanisms of calcium–silicate–hydrate: an overview of recent advances and challenges," *International Journal of Concrete Structures and Materials,* vol. 9, no. 4, pp. 453-462, 2015.

[24] A. Morshedifard, S. Masoumi and M. A. Qomi, "Nanoscale origins of creep in calcium silicate hydrates," *Nature Communications,* vol. 9, no. 1, pp. 1-10, 2018.

[25] S. S. Ray and M. Okamoto, "Polymer/layered silicate nanocomposites: a review from preparation to processing," *Progress in Polymer Science,* vol. 28, no. 11, pp. 1539-1641, 2003.

[26] F. Hussain, M. Hojjati, M. Okamoto and R. E. Gorga , "Polymer-matrix nanocomposites, processing, manufacturing, and application: an overview," *Journal of Composite Materials,* vol. 40, no. 17, pp. 1511-1575, 2006.

[27] H. Matsuyama and J. F. Young, "Intercalation of polymers in calcium silicate hydrate: a new synthetic approach to biocomposites?," *Chemistry of Materials ,* vol. 11, no. 1, pp. 16-19, 1999.

[28] A. Popova, G. Ghita , M.-F. Renou-Gonnord, P. Faucon and E. Gartner, "Interactions between polymeric dispersants and calcium silicate hydrates," *Journal of the American Ceramic Society,* vol. 83, no. 10, pp. 2556-2560, 2000.

[29] S. C. Mojumdar and L. Raki, "Preparation and properties of calcium silicate hydrate-poly (vinyl alcohol) nanocomposite materials," *Journal of Thermal Analysis and Calorimetry,* vol. 82, no. 1, pp. 89-85, 2005.

[30] S. C. Mojumdar and L. Raki, "Preparation, thermal, spectral and microscopic studies of calcium silicate hydrate-poly (acrylic acid) nanocomposite materials," *Journal of Thermal Analysis and Calorimetry,* vol. 85, no. 1, pp. 99-105, 2006.

[31] J. J. Beaudoin, L. Raki and R. Alizadeh, "A ^{29}Si MAS NMR study of modified C-S-H nanostructures," *Cement and Concrete Composites,* vol. 31, no. 8, pp. 585-590, 2009.

[32] R. Alizadeh, J. J. Beaudoin, L. Raki and V. Terskikh, "C-S-H/polyaniline nanocomposites prepared by in situ polymerization," *Journal of Materials Science,* vol. 46, no. 2, pp. 460-467, 2011.

[33] R. Khoshnazar, J. J. Beaudoin, L. Raki and R. Alizadeh, "Interaction of 2-, 3-and 4-nitrobenzoic acid with the structure of calcium–silicate–hydrate," *Materials and Structures,* vol. 49, no. 1, pp. 499-506, 2016.

[34] J. Plank and C. Hirsch, "Impact of zeta potential of early cement hydration phases on superplasticizer adsorption," *Cement and Concrete Research,* vol. 37, no. 4, pp. 537-542, 2007.

[35] J. Plank, Z. Dai and N. Zouaoui, "Novel hybrid materials obtained by intercalation of organic comb polymers into Ca–Al–LDH," *Journal of Physics and Chemistry of Solids,* vol. 69, no. 5-6, pp. 1048-1051, 2008.

[36] J. Plank, K. Pöllmann, N. Zouaoui, P. R. Andres and C. Schaefer, "Synthesis and performance of methacrylic ester based polycarboxylate superplasticizers possessing

hydroxy terminated poly (ethylene glycol) side chains," *Cement and Concrete Research,* vol. 38, no. 10, pp. 1210-1216, 2008.

[37] J. Plank, Z. Dai , H. Keller, F. V. Hössle and W. Seidl, "Fundamental mechanisms for polycarboxylate intercalation into C_3A hydrate phases and the role of sulfate present in cement," *Cement and Concrete Research,* vol. 40, no. 1, pp. 45-47, 2010.

[38] A. Habbaba, A. Lange and J. Plank, "Synthesis and performance of a modified polycarboxylate dispersant for concrete possessing enhanced cement compatibility," *Journal of Applied Polymer Science,* vol. 129, no. 1, pp. 346-353, 2013.

[39] L. Lei and J. Plank, "Synthesis and properties of a vinyl ether-based polycarboxylate superplasticizer for concrete possessing clay tolerance," *Industrial & Engineering Chemistry Research,* vol. 53, no. 3, pp. 1048-1055, 2014.

[40] V. Kanchanason and J. Plank, "Role of pH on the structure, composition and morphology of CSH-PCE nanocomposites and their effect on early strength development of Portland cement," *Cement and Concrete Research,* vol. 102, pp. 90-98, 2017.

[41] G. Geng, R. J. Myers, M. J. A. Qomi and P. J. Monteiro, "Densification of the interlayer spacing governs the nanomechanical properties of calcium-silicate-hydrate," *Scientific Reports,* vol. 7, no. 1, pp. 1-8, 2017.

[42] P. Hosseini, R. Hosseinpourpia, A. Pajum, M. M. Khodavirdi, H. Izadi and A. Vaezi, "Effect of nano-particles and aminosilane interaction on the performances of cement-based composites: An experimental study," *Construction and Building Materials,* vol. 66, pp. 113-124, 2014.

[43] J. Minet, S. Abramson, B. Bresson, A. Franceschini, H. Van Damme and N. Lequeux, "Organic calcium silicate hydrate hybrids: a new approach to cement based nanocomposites," *Journal of Materials Chemistry,* vol. 16, no. 14, pp. 1379-1383, 2006.

[44] C. A. Orozco, "Determination of structural changes, bonds character and mechanical properties of the materials formed by the interaction between C-S-H and soluble organic compounds," PhD thesis, University of California Berkeley, 2017.

[45] C. A. Orozco, B. W. Chun, G. Geng, A. H. Emwas and P. J. Monteiro, "Characterization of the bonds developed between calcium silicate hydrate and polycarboxylate-based superplasticizers with silyl functionalities," *Langmuir,* vol. 33, no. 14, pp. 3404-3412, 2017.

[46] C. A. Casagrande, L. F. Jochem, L. Onghero, P. R. de Matos, W. L. Repette and P. J. P. Gleize, "Effect of partial substitution of superplasticizer by silanes in Portland cement pastes," *Journal of Building Engineering,* vol. 29, p. 101226, 2020.

[47] Z. Zhu, Z. Wang, Y. Zhou, Y. Wei and A. She, "Synthesis and structure of calcium silicate hydrate (CSH) modified by hydroxyl-terminated polydimethylsiloxane (PDMS)" *Construction and Building Materials,* vol. 267, p. 120731, 2021.

[48] A. Stewart, B. Schlosser and E. P. Douglas, "Surface modification of cured cement pastes by silane coupling agents," *ACS Applied Materials & Interfaces,* vol. 5, no. 4, pp. 1218-1225, 2013.

[49] J. S. Vasconcellos, G. L. O. Martins, G. D. A. R. Oliveira, L. M. Lião, J. H. da Silva Rêgo and P. P. C. Sartoratto, "Effect of amine functionalized nanosilica on the cement hydration and on the physical-mechanical properties of Portland cement pastes," *Journal of Nanoparticle Research,* vol. 22, no. 8, pp. 1-13, 2020.

[50] P.-C. Aïtcin and R. J. Flatt, Science and technology of concrete admixtures, Woodhead Publishing, 2015.

[51] C. Gay and E. Raphael, "Comb-like polymers inside nanoscale pores," *Advances in Colloid and Interface Science,* vol. 94, no. 1-3, pp. 229-236, 2001.

[52] D. Marchon, "Controlling cement hydration through the molecular structure of comb copolymer superplasticizers," PhD thesis, ETH Zurich, 2016.

[53] D. Attwood, Soft x-rays and extreme ultraviolet radiation: principles and applications, Cambridge university press, 2000.

[54] A. J. Seibert and J. M. Boone, "X-ray imaging physics for nuclear medicine technologists. Part 2: X-ray interactions and image formation," *Journal of Nuclear Medicine Technology,* vol. 33, no. 1, pp. 3-18, 2005.

[55] B. D. Cullity, Elements of x-ray diffraction, Addison-Wesley Publishing, 1956.

[56] G. S. Girolami, X-ray crystallography, University Science Books, 2016.

[57] P. Willmott, An introduction to synchrotron radiation: techniques and applications, John Wiley & Son, 2019.

[58] S. Merkel, A. Kubo, L. Miyagi, S. Speziale, T. S. Duffy, H.-k. Mao and H.-R. Wenk, "Plastic Deformation of $MgGeO_3$ Post-Perovskite at Lower Mantle Pressures," *Science ,* vol. 311, no. 5761, pp. 644-646, 2006.

[59] H. R. Wenk, I. Lonardelli, S. Merkel, L. Miyagi, J. Pehl, S. Speziale and C. E. Tommaseo, "Deformation textures produced in diamond anvil experiments, analysed in radial diffraction geometry," *Journal of Physics: Condensed Matter,* vol. 18, no. 25, p. S933, 2006.

[60] S. M. Clark, B. Colas, M. Kunz, S. Speziale and P. J. Monteiro, "Effect of pressure on the crystal structure of ettringite," *Cement and Concrete Research,* vol. 38, no. 1, pp. 19-26, 2008.

[61] J. E. Oh, S. M. Clark and P. J. Monteiro, "Does the Al substitution in C–S–H (I) change its mechanical property?" *Cement and Concrete Research,* vol. 41, no. 1, pp. 102-106, 2011.

[62] J. H. Moon, J. E. Oh, M. Balonis, F. P. Glasser, S. M. Clark and P. J. Monteiro, "Pressure induced reactions amongst calcium aluminate hydrate phases," *Cement and Concrete Research,* vol. 41, no. 6, pp. 571-578, 2011.

[63] J. Moon, S. Yoon, R. M. Wentzcovitch, S. M. Clark and P. J. Monteiro, " Elastic properties of tricalcium aluminate from high-pressure experiments and first-principles calculations," *Journal of the American Ceramic Society,* vol. 95, no. 9, pp. 2972-2978, 2012.

[64] J. E. Oh, S. M. Clark, H. R. Wenk and P. J. Monteiro, "Experimental determination of bulk modulus of 14 Å tobermorite using high pressure synchrotron X-ray diffraction," *Cement and Concrete Research,* vol. 42, no. 2, pp. 397-403, 2012.

[65] J. Moon, J. E. Oh, M. Balonis, F. P. Glasser, S. M. Clark and P. J. Monteiro, "High pressure study of low compressibility tetracalcium aluminum carbonate hydrates $3CaO\cdot Al_2O_3\cdot CaCO_3\cdot 11H_2O$," *Cement and Concrete Research,* vol. 42, no. 1, pp. 105-110, 2012.

[66] M. D. Jackson, J. Moon, E. Gotti, R. Taylor, S. R. Chae, M. Kunz and P. J. Monteiro, "Material and elastic properties of Al-tobermorite in ancient Roman seawater concrete," *Journal of the American Ceramic Society,* vol. 96, no. 8, pp. 2598-2606, 2013.

[67] C. W. Hargis, J. Moon, B. Lothenbach, F. Winnefeld, H. R. Wenk and P. J. Monteiro, "Calcium sulfoaluminate sodalite ($Ca_4Al_6O_{12}SO_4$) crystal structure evaluation and bulk modulus determination," *Journal of the American Ceramic Society,* vol. 97, no. 3, pp. 892-898, 2014.

[68] J. Moon, S. Yoon and P. J. Monteiro, "Mechanical properties of jennite: A theoretical and experimental study," *Cement and Concrete Research,* vol. 71, pp. 106-114, 2015.

[69] G. Geng, R. N. Nikolayevich , J. Li, M. J. Qomi, J. Yan, H.-R. Wenk and P. J. Monteiro, "Preferred orientation of calcium aluminosilicate hydrate induced by confined compression," *Cement and Concrete Research,* vol. 113, pp. 186-196, 2018.

[70] G. Geng, J. Li, Y. Zhou, L. Liu, J. Yan, M. Kunz and P. J. Monteiro, "A high-pressure X-ray diffraction study of the crystalline phases in calcium aluminate cement paste," *Cement and Concrete Research,* vol. 108, pp. 38-45, 2018.

[71] H. L. Monaco, G. Artioli, D. Viterbo, G. Ferraris, G. Gilli, G. Zanotti and M. Catti, Fundamentals of crystallography, Oxford university press, USA, 2002.

[72] E. Boldyreva and P. Dera, High-pressure crystallography: from fundamental phenomena to technological applications, Springer Science & Business Media, 2010.

[73] Y. Wang, W. B. Durham and I. C. Getting, "The deformation-DIA: A new apparatus for high temperature triaxial deformation to pressures up to 15 GPa," *Review of Scientific Instruments,* vol. 74, no. 6, pp. 3002-3011, 2003.

[74] H. R. Wenk, G. Ischia, N. Nishiyama, Y. Wang and T. Uchida, "Texture development and deformation mechanisms in ringwoodite," *Physics of the Earth and Planetary Interiors,* vol. 152, no. 3, pp. 191-199, 2005.

[75] H.-R. Wenk and S. Grigull , "Synchrotron texture analysis with area detectors," *Journal of Applied Crystallography,* vol. 36, no. 4, pp. 1040-1049, 2003.

[76] H. R. Wenk, S. Matthies, J. Donovan and D. Chateigner, "BEARTEX: a Windows-based program system for quantitative texture analysis," *Journal of Applied Crystallography,* vol. 31, no. 2, pp. 262-269, 1998.

[77] L. Lutterotti, S. Matthies, H. R. Wenk, A. S. Schultz and J. W. Richardson Jr, "Combined texture and structure analysis of deformed limestone from time-of-flight neutron diffraction spectra," *Journal of Applied Physics,* vol. 81, no. 2, pp. 594-600, 1997.

[78] L. Lutterotti, R. Vasin and H.-R. Wenk, "Rietveld texture analysis from synchrotron diffraction images. I. Calibration and basic analysis," *Powder Diffraction,* vol. 29, no. 1, pp. 76-84, 2014.

[79] H. R. Wenk, L. Lutterotti, P. Kaercher, W. Kanitpanyacharoen, L. Miyagi and R. Vasin, "Rietveld texture analysis from synchrotron diffraction images. II. Complex multiphase materials and diamond anvil cell experiments," *Powder Diffraction,* vol. 29, no. 3, pp. 220-232, 2014.

[80] G. B. Jeffery, "The motion of ellipsoidal particles immersed in a viscous fluid," *Proceedings of the Royal Society of London. Series A, Containing Papers of a Mathematical and Physical Character,* vol. 102, no. 715, pp. 161-179, 1922.

[81] A. March, "Mathematische Theorie der Regelung nach der Korngestah bei affiner Deformation," *Zeitschrift für Kristallographie-Crystalline Materials,* vol. 81, no. 1-6, pp. 285-297, 1932.

[82] W. A. Dollase, "Correction of intensities for preferred orientation in powder diffractometry: application of the March model," *Journal of Applied Crystallography,* vol. 19, no. 4, pp. 267-272, 1986.

[83] K. Nagao and E. Kagami, "X-ray thin film measurement techniques VII. Pole figure measurement," *Rigaku J ,* vol. 27, no. 2, pp. 6-14, 2011.

[84] D. o. M. S. &. Metallurgy, "Dissemination of IT for the Promotion of Materials Science (DoITPoMS)," University of Cambridge, 2004-2021. [Online]. Available: https://www.doitpoms.ac.uk/tlplib/crystallographic_texture/texture_representation.php. [Accessed 25 11 2021].

[85] F. Birch, "Elasticity and constitution of the Earth's interior," *Journal of Geophysical Research,* vol. 57, no. 2, pp. 227-286, 1952.

[86] J. E. Oh, S. M. Clark, H.-R. Wenk and P. J. Monteiro, "Experimental determination of bulk modulus of 14 Å tobermorite using high pressure synchrotron X-ray diffraction," *Cement and Concrete Research,* vol. 42, no. 2, pp. 397-403, 2012.

[87] T. Mitsuda and H. F. W. Taylor, "Influence of aluminium on the conversion of calcium silicate hydrate gels into 11 Å tobermorite at 90 C and 120 C," *Cement and Concrete Research,* vol. 5, no. 3, pp. 203-209, 1975.

[88] C. T. Prewitt and R. T. Downs, "High-pressure crystal chemistry," *Ultrahigh Pressure Mineralogy,* pp. 283-318, 2018.

[89] S. Matthies and G. W. Vinel, "On the reproduction of the orientation distribution function of texturized samples from reduced pole figures using the conception of a conditional ghost correction," *Physica Status Solidi,* vol. 112, no. 2, pp. 111-114, 1982.

[90] F. H. Wittmann, "Interaction of hardened cement paste and water," *Journal of the American Ceramic Society,* vol. 56, no. 8, pp. 409-415, 1973.

[91] P. Klug and F. H. Wittmann, "Activation energy and activation volume of creep of hardened cement paste," *Materials Science and Engineering,* vol. 15, no. 1, pp. 63-66, 1974.

[92] W. Ruetz, "A hypothesis for the creep of hardened cement paste and the influence of simultaneous shrinkage," *Proceedings of the Structure of Concrete and its Behavior under Load,* pp. 365-387, 1968.

[93] D. W. Gardner, J. Li, A. Morshedifard, S. Masoumi, M. J. A. Qomi, P. J. M. Monteiro, R. Maboudian and C. Carraro, "Silicate bond characteristics in calcium–silicate–hydrates determined by high pressure Raman spectroscopy," *The Journal of Physical Chemistry C,* vol. 124, no. 33, pp. 18335-18345, 2020.

Appendix

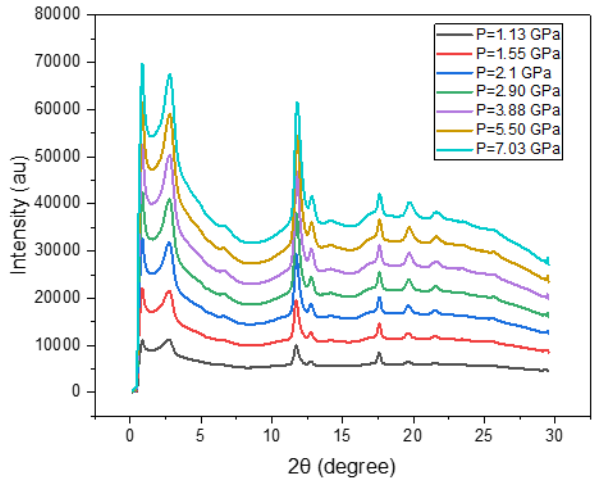

Figure 59 DAC measurements of the CSH-PCE sample at different hydrostatic pressures

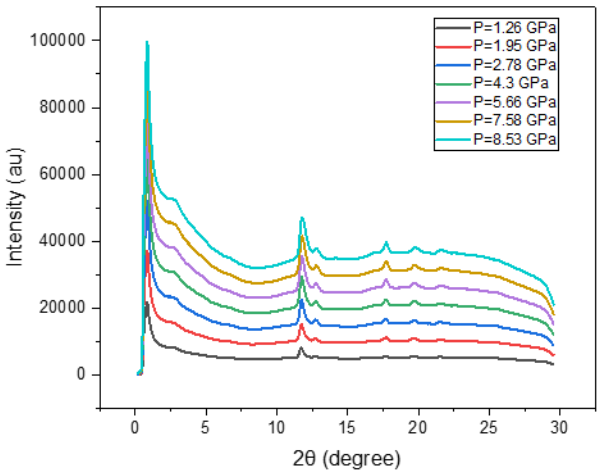

Figure 60 DAC measurements of the CSH-APTES A sample at different hydrostatic pressures

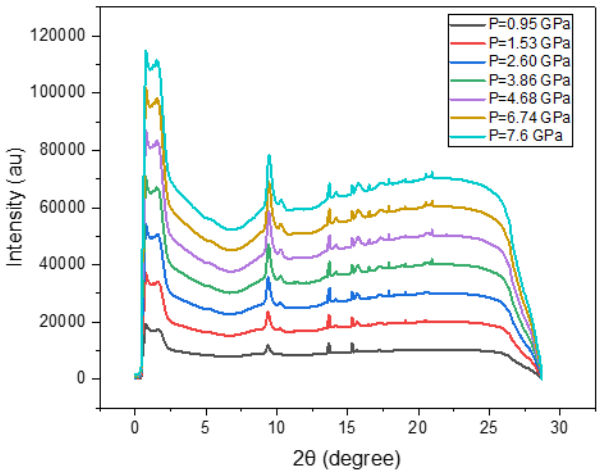

Figure 61 DAC measurements of the CSH-APTES B sample at different hydrostatic pressures